

# **Searches for Supersymmetry with compressed mass spectra using monojet events with the CMS detector at the LHC**

Robyn Elizabeth Lucas  
Imperial College London

A dissertation submitted to Imperial College London  
for the degree of Doctor of Philosophy

## Abstract

This is the abstract, find me in frontmatter.tex

## Declaration

I, the author of this thesis, hereby declare the material presented here to be the result of my own work, except where explicit reference is made to the work of others. It has not been submitted for another qualification to this or any other university. All figures labelled “CMS” have been sourced from CMS publications, referenced in the caption, and include those produced by the author. Those figures labelled “CMS Preliminary” have been sourced from a CMS public preliminary document or an unpublished CMS document. All figures taken from external sources are referenced appropriately throughout this thesis.

Robyn Lucas

## Acknowledgements

# Contents

<b>1</b>	<b>Introduction</b>	<b>2</b>
<b>2</b>	<b>Theory and Motivations</b>	<b>3</b>
2.1	The Standard Model of Particle Physics	3
2.1.1	Fundamental particles and forces	5
2.1.2	Gauge Symmetries	7
2.1.3	Electroweak Symmetry Breaking and the Higgs	7
2.2	Motivation for Physics Beyond the Standard Model	7
2.3	Supersymmetry	7
2.3.1	Compressed Supersymmetry	7
<b>3</b>	<b>The LHC and CMS experiment</b>	<b>8</b>
3.1	The LHC	8
3.2	The CMS Detector	10
3.2.1	The Tracking System	12
3.2.2	The Electromagnetic Calorimeter	13
3.2.3	The Hadronic Calorimeter	15
3.2.4	The Muon System	17
3.3	Event Reconstruction	20
3.3.1	Jets	21
3.3.2	Missing Transverse Energy	24
3.3.3	Muons	24
3.4	The Trigger	26
3.4.1	The L1 Trigger	27
3.4.2	The High Level Trigger	29
<b>4</b>	<b>Jet Algorithms for the L1 Trigger Upgrade</b>	<b>30</b>
4.1	The LHC Upgrade	30

4.2	CMS Trigger Upgrade . . . . .	33
4.2.1	Calorimeter Trigger Upgrade . . . . .	33
4.3	Algorithm for jet reconstruction at L1 . . . . .	36
4.3.1	Jet Reconstruction . . . . .	37
4.3.2	Jet Filtering . . . . .	39
4.3.3	Event-by-event estimation of pile-up . . . . .	40
4.3.4	Calibration to the jet energy scale . . . . .	41
4.4	Upgrade L1 Jet Algorithm Performance . . . . .	42
4.4.1	Angular and Energy Resolutions . . . . .	43
4.4.2	Trigger efficiencies . . . . .	44
4.4.3	Jet trigger rates . . . . .	46
4.4.4	Other jet variables . . . . .	47
4.5	Conclusion . . . . .	50
5	<b>Searching for Compressed SUSY with monojet events</b>	52
5.1	Analysis . . . . .	52
6	<b>Searching for Compressed SUSY with monojet events in parked data</b>	53
	<b>Bibliography</b>	55
	<b>List of Figures</b>	59
	<b>List of Tables</b>	64
1	Acronyms . . . . .	64

*“For Peter”*

---

# Chapter 1

## Introduction

*“Everything starts somewhere, although many physicists disagree.”*

— Terry Pratchet

# Chapter 2

## Theory and Motivations

*“Absence of evidence is not evidence of absence.”*

— Carl Sagan, 1934 - 1996

This chapter introduces the Standard Model (SM) as a gauge invariant Quantum Field Theory (QFT), and gives a description of the fundamental particles and their interactions. The shortcomings of the SM, outlined in Section 2.2, imply however that it must be an incomplete description of nature. A Supersymmetric extension of the SM can address many of these limitations and is described in Section 2.3. Particular emphasis is placed on the arguments for SUperSYmmetry (SUSY) with compressed mass spectra in Section 2.3.1, as this is the subject of this thesis. The convention  $c = \bar{h} = 1$  is used throughout. The four vector indices are labelled  $\mu$  and  $\nu$ . The  $SU(2)$  generators are labelled  $i$ ,  $j$ , and  $k$ , while the  $SU(3)$  generators are labelled  $a$ ,  $b$ , and  $c$ . Gravity, of order  $10^{33}$  times weaker than the forces discussed in this chapter, is neglected. The lack of any explanation of gravity within the SM suggests its incompleteness as a total description of nature.

### 2.1 The Standard Model of Particle Physics

The SM of particle physics provides a fantastically accurate description of the fundamental particles of nature and their interactions via the strong, electromagnetic, and weak forces at the electroweak energy scale. It has proved itself incredibly robust during the first years of Large Hadron Collider (LHC) running. Many high precision measurements are

consistent with their loop level SM predictions, see Figure 2.1, which shows experiment and theory expectations agree over 6 orders of magnitude, across many different processes. Even very rare processes have been measured to agree with their SM predictions: the decay  $B_S \rightarrow \mu\mu$ , very sensitive to new physics processes, has been observed at the level of three in every billion decays of the  $B_S$  meson [1]. Such tests of the SM cement its place as one of the major successes of 20<sup>th</sup> century physics.

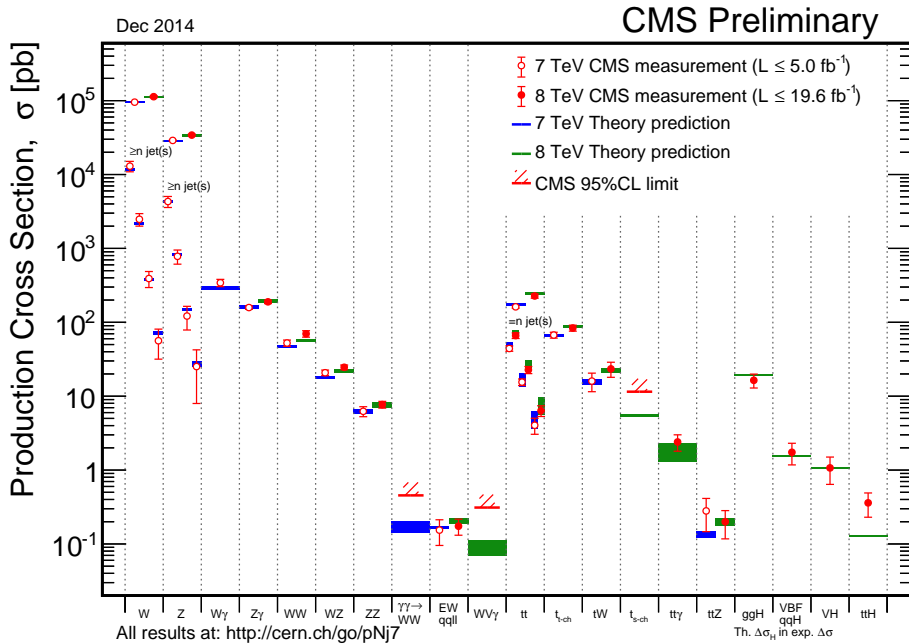


**Figure 2.1:** Combined results from CMS of many SM measurements made at LHC centre-of-mass energies of 7 and 8 TeV, taken from [2]. Theory and experiment agree over a vast range of production cross section values, for many different SM processes.

Developed in the 1960's and 1970's [3–6], the SM is a relativistic QFT in which particles are excitations of fields. It is gauge invariant, guaranteeing its renormalizability, and contains three symmetries:  $SU(3)_C \times SU(2)_L \times U(1)_Y$ .  $SU(3)$  describes the strong force, felt by coloured particles, and  $SU(2) \times U(1)$  describes the unified Electromagnetic and Weak forces, felt by particles with weak isospin and weak hypercharge. The Higgs mechanism [7] describes the spontaneous symmetry breaking of the  $SU(2) \times U(1)$  gauge symmetry which allows massive gauge bosons in a gauge invariant way. The discovery of the Higgs boson [8, 9] in July 2012, the mediator of the Higgs field, provided the last piece of the SM.

### 2.1.1 Fundamental particles and forces

All known matter in the universe can be described by the fundamental matter particles, which can be separated into quarks - those that feel the strong force, and leptons - those that do not. Matter particles are all spin- $\frac{1}{2}$  fermions that conform to Fermi statistics and obey the Dirac equation:

$$(i\gamma^\mu \delta_\mu - m)\phi = 0, \quad (2.1)$$

where  $\gamma^\mu$  are the Dirac matrices, which are defined by their anti-commutation relation  $\{\gamma^\mu, \gamma^\nu\} = \gamma^\mu \gamma^\nu + \gamma^\nu \gamma^\mu = 2\eta^{\mu\nu} I_4$ , where  $\eta^{\mu\nu}$  is the Minkowski metric  $(+, -, -, -)$ , and  $I_4$  is the four-dimensional identity matrix;  $\delta_\mu$  is the covariant derivative; and  $m$  is the mass of the particle. Repeated indices are summed over [10].

A summary of the matter particles of the SM can be found in Table 2.1. A similar table exists for the antiparticles of the leptons and quarks, a consequence of Equation 2.1, which has both positive and negative energy solutions. Rather than particles travelling backwards through time, as the negative energy solutions suggest, anti-particles are interpreted to have all of the same properties as their partner particles but with opposite charge.

Leptons are fundamental, free particles in nature. Conversely, quarks are fundamental but not free particles; they form hadrons: baryons, which consist of 3 quarks or anti-quarks, and mesons, a bound quark-anti-quark pair. This difference is due to the colour charge that quarks carry: they interact with the strong force, whereas the colourless leptons do not.

Matter particles interact via the exchange of spin-1 gauge bosons. The photon  $\gamma$  mediates the electromagnetic interaction and the heavy  $W^\pm$  and  $Z$  bosons mediate the weak interaction, through the mixing of the gauge fields when the respective forces are unified. There are 8 colourless gluons ( $g$ ) that mediate the strong force. The properties of these bosons, and similarly the properties of the interactions, are a direct result of their gauge symmetry groups, detailed in Section 2.1.2. A summary of the bosons can be found in Table 2.2.

The electron was discovered by J.J. Thomson in the Canvendish Laboratory in 1897, and the electron (anti)-neutrino was first proposed by Pauli in 1930 to explain

Matter fermions: spin- $\frac{1}{2}$						
Generation	Leptons			Quarks		
	Particle	Mass (MeV)	Charge	Particle	Mass (MeV)	Charge
1	$\nu_e$	0	0	d	2.3	$-\frac{1}{3}$
	e	0.511	-1	u	4.8	$+\frac{2}{3}$
2	$\nu_\mu$	0	0	s	95	$-\frac{1}{3}$
	$\mu$	106	-1	c	1270	$+\frac{2}{3}$
3	$\nu_\tau$	0	0	b	4180	$-\frac{1}{3}$
	$\tau$	1780	-1	t	173000	$+\frac{2}{3}$

**Table 2.1:** Summary of the particles of the SM of particle physics. Fermions, of spin- $\frac{1}{2}$  are shown, split into the three generations of leptons and quarks.

Force carrying gauge bosons: spin-1					
Force	Particle	Symbol	Mass (GeV)	Charge	
Electromagnetic	Photon	$\gamma$	0	0	
	W boson	$W^+$	80.4	1	
Weak	W boson	$W^-$	80.4	-1	
	Z boson	Z	91.2	0	
Strong	Gluons (8)	$g$	0	0	
Higgs Boson: spin-0					
-	Higgs	$H^0$	126	0	

**Table 2.2:** Summary of the gauge bosons of the SM. The force carrying bosons of spin-1 are shown, with the Higgs boson to complete the picture.

the energy spectrum of beta decay, though it was not discovered until 1956 by Cowan and Reines at Los Alamos [11]. The muon was discovered in 1936 by Anderson and Neddermeyer at Caltech in studies of cosmic rays, and confirmed a year later in a cloud chamber experiment. The muon neutrino was then discovered in 1962 by Lederman, Schwartz and Steinberger, after being proposed in the early 1940s. The  $u$ ,  $d$ , and  $s$  quarks were first proposed in 1964 by Gell-Man and Zweig to explain the ‘Eightfold’ hadron structure [12, 13], and the three quarks were observed in deep inelastic scattering experiments at the Stanford Linear Accelerator Center (SLAC) 4 years later. The proposal of the GIM mechanism [14] in 1970 predicted the completion of the second generation - the charm quark in order to explain the observed suppression of Flavour Changing Neutral Currents (FCNC)s. The third generation was more of a surprise - the

$\tau$  lepton was proposed to explain an excess of events at the  $e^+e^-$  colliding ring at SLAC in the mid 1970's, and the  $\nu_\tau$  was not discovered until 2000, completing the lepton family. CP violation in kaon decay drove the proposal of the third quark generation in 1973 [15]. The bottom quark was first observed in 1977. The top quark, after years of dedicated searches, was not discovered until 1995 at the Tevatron. The SM was thus built as a theory over several decades; driven by the need to explain experimental observations, predicting the existence of particles that were then found later after dedicated searches.

### 2.1.2 Gauge Symmetries

### 2.1.3 Electroweak Symmetry Breaking and the Higgs

## 2.2 Motivation for Physics Beyond the Standard Model

## 2.3 Supersymmetry

### 2.3.1 Compressed Supersymmetry

# Chapter 3

## The LHC and CMS experiment

*“Insanity: doing the same thing over and over again and expecting different results.”*

— Albert Einstein, 1879 - 1955

Probing the physics of the SM and beyond at the TeV scale is only possible with the technologically unparalleled apparatus situated at the European Organisation for Nuclear Research (CERN). This chapter will introduce the hugely complex machinery of the LHC, which provides proton-proton collisions at centre-of-mass energies in excess of  $\sqrt{s} = 7$  TeV, and outline the main features of the CMS experiment, of which the author is a member, with particular focus on those features relevant to the material presented in this thesis. Section 3.1 presents the main features of the LHC, and Section 3.2 provides an overview of the CMS detector. Physics object reconstruction is described in Section 3.3 and the CMS trigger system is discussed in Section 3.4.

### 3.1 The LHC

The LHC is the world’s largest and most energetic synchrotron particle collider. Housed in the tunnel built for the Large Electron-Positron Collider (LEP) collider that operated during the 1990’s at CERN, the LHC is a double ring circular collider 27 km in circumference, and sits on the bedrock beneath the Franco-Swiss border, close to Geneva, Switzerland. It is designed for both proton-proton (pp) and heavy ion (PbPb) collisions at a centre of mass energy  $\sqrt{s} = 14$  TeV and luminosity of  $10^{34}\text{cm}^{-2}\text{s}^{-1}$ .

Currently the world's only operating collider able to study physics directly at the TeV scale, the LHC consists of thousands of superconducting magnets which act to accelerate, bend and focus two beams of protons (or heavy ions) that circulate in opposite directions around the accelerator. A chain of accelerators, shown in Figure 3.1 and culminating with the Super Proton Synchrotron (SPS), inject bunches of approximately one hundred billion protons 25 or 50 ns apart at  $\sqrt{s} = 450$  GeV into the two beams of LHC. Oscillating electric fields provided by 1232 superconducting dipole magnets act to accelerate the beams up to the operating centre of mass energy, which for the data used in this thesis was  $\sqrt{s} = 8$  TeV, with bunch crossings every 50 ns. Once protons are accelerated to the operational  $\sqrt{s}$ , the LHC acts as a storage ring, and collisions can occur. Either side of four points around the LHC ring, very high precision magnetic fields, provided by quadrupole and higher order multipole magnets, position and focus the beams such that each bunch has a diameter of  $16 \mu\text{m}$ . The chance of a pp collision with large momentum transfer at the four interaction points around the LHC ring is thereby increased, and the number of such collisions per bunch crossing, termed pile-up (PU) for the data used in this thesis was  $\sim 20$ .

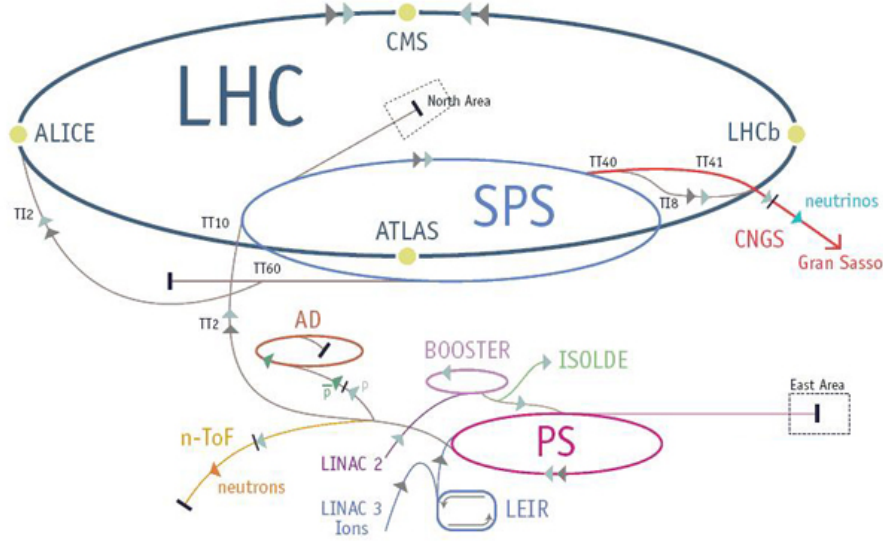


**Figure 3.1:** The LHC accelerator ring, showing the locations of the four main experiments at the four collision points.

Interaction points are at the centre of four large particle detectors, shown in Figure 3.1: A Large Ion Collider Experiment (ALICE) [16], A Toroidal LHC ApparatuS (ATLAS) [17], CMS [18] and Large Hadron Collider Beauty (LHCb) [19]. They act to identify particles produced as a result of a pp or PbPb bunch crossing through a combination of tracking

and calorimetry, in order to reconstruct and measure physical processes, to test currently accepted theories and search for new physics.

### 3.2 The CMS Detector

The CMS detector is a general purpose particle detector situated at Point 5 on the LHC ring, designed to carry out many different measurements for various physics goals. Close to  $4\pi$  solid angle reconstruction with efficient particle identification and reconstruction allows measurements of photons, muons, electrons, taus, hadronic showers and missing transverse momentum. A diagram of CMS is shown in Figure 3.2. It is 21.6 m long, 14.6 m in diameter and weighs 12500 T. It consists of different sub-detectors, each of which measures a different particle or property, and is built around a central 12.5 m long 4 T superconducting solenoid magnet and its iron return yoke. CMS consists of a barrel region, containing the solenoid, and endcaps to extend the forward and backward coverage.

The different sub-detectors are arranged in an onion structure. Closest to the beam line is the silicon tracking system. A very highly resolution pixel detector lies closest to the interaction region, followed by a granular strip detector. Charged particle momenta measurements are made using the curvature of tracks in the uniform magnetic field provided by the solenoid, as well as measurements of displaced vertices and impact parameters which are essential for identifying heavy flavor decays. Energy measurements are provided by the calorimeters, which lie outside the tracker; the Electromagnetic Calorimeter (ECAL) and Hadronic Calorimeter (HCAL). The highly granular ECAL consists of 70,000 transparent lead tungstate crystals. As electrons and photons pass through, they cause electromagnetic showers in the crystals, which produce scintillation light. The sampling HCAL consists of slabs of brass interleaved with plastic. Incident hadrons shower when passing through the absorber (brass), causing scintillation light to be produced in the active material (plastic) as the shower passes through. Scintillation light produced in the crystals, or plastic, is collected by photodetectors and used to infer the incident particle energy and position. The solenoid lies outside the HCAL and provides a 3.8 T axial magnetic field. Embedded in the iron return yoke of the magnet sits the muon system. Three different types of muon detectors are used to identify muons and make momentum and charge measurements over a large kinematic range. More information on the CMS detector can be found in Ref. [18].

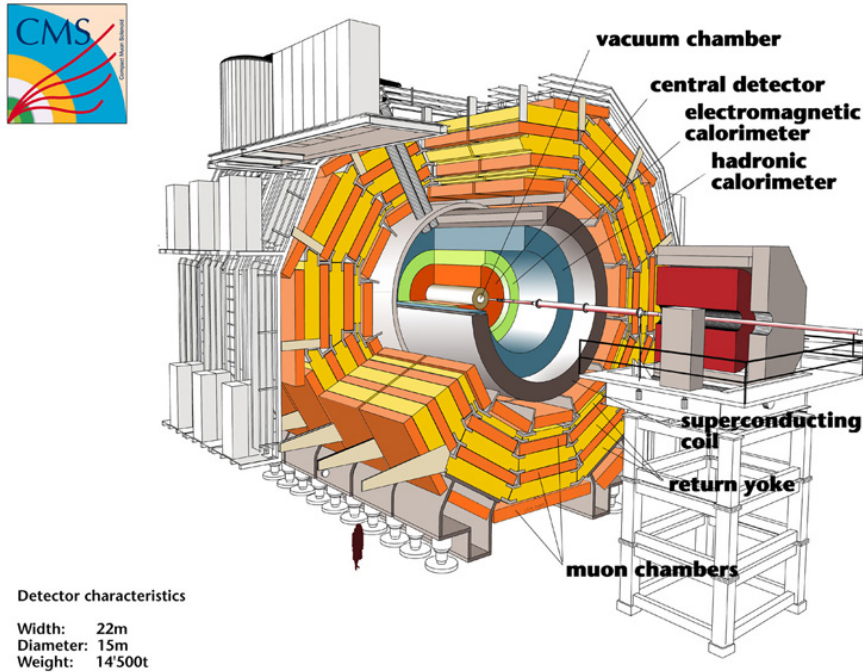


**Figure 3.2:** The CMS detector, with the main subsystems labelled.

CMS uses a right-handed coordinate system: the  $x$ -axis points south towards the centre of the LHC ring, the  $y$ -axis points vertically upwards and the  $z$ -axis is in the direction of the beam, where positive  $z$  is to the West. More natural is the coordinate system defined in terms of  $r$ ,  $\phi$  and  $\theta$ . The azimuthal angle  $\phi$  is measured from the  $x$ -axis in the  $xy$  plane, where the radial component is denoted  $r$ . The polar angle  $\theta$  is defined in the  $rz$  plane, and the pseudorapidity

$$\eta = -\ln \tan(\theta/2). \quad (3.1)$$

Convention is that the position of a particle is described in terms of  $\eta$  and  $\phi$ , where  $\eta = 0$  is along the  $y$ -axis and  $\eta = \infty$  is along the beam direction; and  $-\pi < \phi < \pi$ . The distance between particles is commonly described in terms of the variable  $\Delta R = \sqrt{\Delta\phi^2 + \Delta\eta^2}$ .

The LHC is a hadron collider, and as such, collides non-fundamental particles. Inelastic collisions with large momentum transfer can occur between component quarks and gluons, however in a single bunch crossing there will also be many low energy, elastic, soft scatters, as well as the remnant part of any protons that have had a hard collision. As a result, the forward and backward directions are highly populated environments and therefore difficult to instrument due to high occupancy and radiation damage. CMS has endcaps to extend the detector coverage at high  $\eta$ , however it is not possible to reconstruct the

momentum of a single interaction in the direction of the beam. Additionally, interesting physics is a result of a hard collision, where energy is available for the creation of new particles. It can be characterized by the amount of energy in the transverse ( $xy$ ) plane. For these reasons, particle energy and momenta are described only in the transverse plane, where conservation laws can be applied. By conserving energy and momentum in the transverse plane, any imbalance can be assigned to a particle leaving the detector without any trace; for example from a neutrino, or, from new physics processes such as Dark Matter (DM) production. A nearly hermetic detector (with close to  $4\pi$  coverage in solid angle) allow excellent particle reconstruction and measurements of missing transverse energy, the ‘tell-tale’ sign of new physics, and make CMS perfectly suited to searching for physics beyond the SM.

### 3.2.1 The Tracking System

The tracker is designed for precise and efficient measurement of charged particle trajectories (and therefore position and momentum) as they emerge from the interaction point. Additionally, reconstruction of any secondary vertices is crucial for identifying heavy flavor decays such as jets that originate from b-quarks.

The LHC provides bunch crossings every 25 or 50 ns, resulting in  $\sim 20$  pp interactions, giving rise to of order 1000 particles. All of these traverse the tracker. The granularity of the tracker must be such that one can determine which of the  $\sim 20$  pp vertices each of the particles come from, and the electronics fast enough that the information is sent on in time for the next bunch crossing to arrive. With such high particle fluxes, the tracker is also subject to a huge amount of radiation damage. These conditions must be dealt with using the least amount of material possible in order to limit multiple scattering, photon conversion, bremsstrahlung and nuclear interactions. To meet such criteria, and to have an estimated lifetime of 10 years, the tracker is constructed entirely from silicon.

The tracker consists of an all silicon pixel and strip detector. Measuring 5.8 m in length and 2.5 m in diameter, with a total active area of  $200 \text{ m}^2$ , it surrounds the interaction region. The pixel detector has three layers in the barrel, at radii of 4.4 cm, 7.3 cm and 10.2 cm. In the endcaps, there are two disks at distances  $z = \pm 34.5, \pm 46.5$  cm. The strip detector has a length of 5.8 m and a diameter of 2.4 m, and is composed of four subsystems: the Tracker Inner Barrel (TIB), Tracker Outer Barrel (TOB), Tracker Inner Disks (TID) and Tracker Endcaps (TEC). The CMS tracker geometry is shown in Figure 3.3.

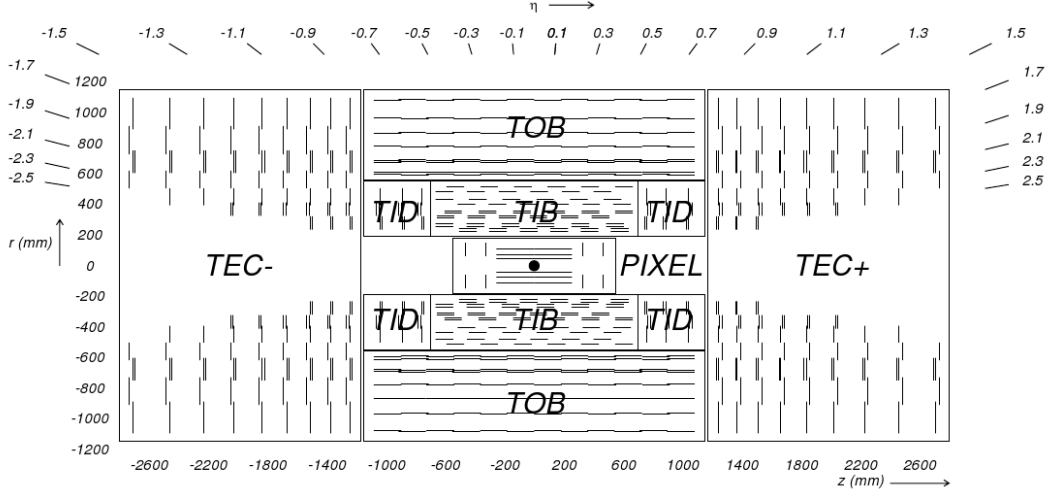


**Figure 3.3:** The CMS tracker, shown in the  $r z$  plane. The pixel detector is shown at the centre of the tracker, closest to the interaction region (shown by the black dot), and the strip detector surrounds it. The different subsystems of the strip detector are shown. Taken from Ref. [18].

The energy resolution of the tracker is shown in Figure 3.4, for samples of single muons with  $p_T$  of 1, 10 and 100 GeV. For a 100GeV muon, the resolution is 1-2% up to  $|\eta| = 1.6$ . Lower momentum objects have a better energy resolution as their tracks have increased curvature.

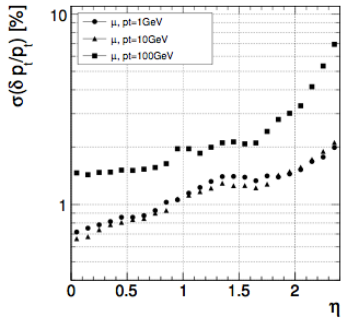


**Figure 3.4:** The energy resolution as a function of  $|\eta|$  for CMS tracker, shown for single muons with  $p_T = 1, 10$  and  $100$  GeV.

### 3.2.2 The Electromagnetic Calorimeter

High resolution photon and electron position and energy measurements are provided by the lead tungstate ( $\text{PbWO}_4$ ) crystal ECAL, which covers pseudorapidity up to  $|\eta| < 3$ . It is made up of the Electromagnetic Calorimeter Barrel (EB), covering the range

$0 < |\eta| < 1.479$ , and the Electromagnetic Calorimeter Endcap (EE), covering the range  $1.479 < |\eta| < 3$ .

Both fast response times (80% of scintillation light is emitted in 25 ns) and radiation hardness are required from the ECAL, motivating the choice of material. In addition, it is very dense ( $8.28 \text{ gcm}^{-3}$ ), has a short radiation length ( $X_0 = 0.89 \text{ cm}$ ), and small Molière radius (2.2 cm), making it well suited to a compact, fine granularity calorimeter. Arranged in a quasi-projective geometry, 61,200 crystals in the barrel and 7,324 crystals in the endcaps are tapered in shape and angled at  $3^\circ$  to ensure that particle trajectories avoid cracks between them. Barrel crystals have a front face of  $22 \times 22 \text{ mm}^2$  and a length of 23 cm, corresponding to  $25.8 X_0$ . Endcap crystals have a front face of  $28.6 \times 28.6 \text{ mm}^2$  and length corresponding to  $24.7 X_0$ . Electromagnetic showers are therefore expected to be contained within one crystal length, so only a single layer of crystals is needed. A preshower detector is placed in front of the endcaps, with a thickness of  $3X_0$ , in the range  $1.653 < |\eta| < 2.6$ , in order to distinguish between single photons and photon pairs resulting from neutral pion decay. The ECAL geometry is shown in Figure 3.5.

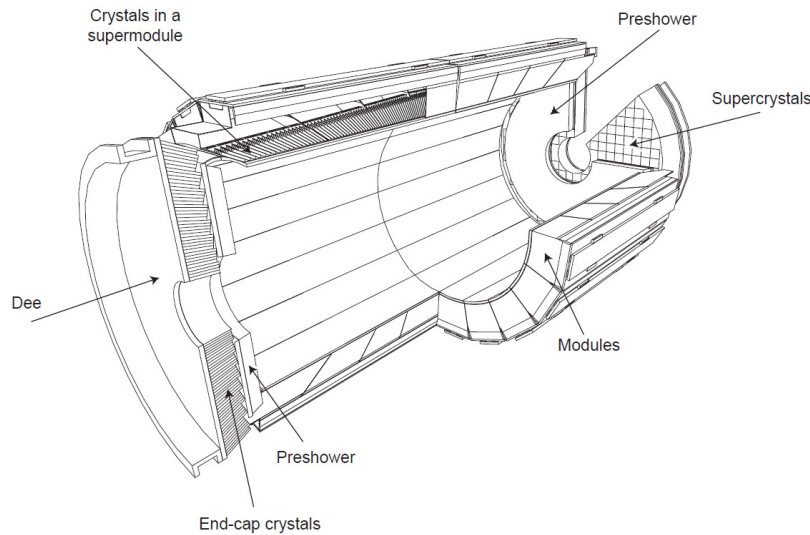


**Figure 3.5:** Geometric view of the CMS ECAL. Barrel crystals are arranged in modules and supermodules, and endcap crystals arranged in supercrystals. Also shown is the preshower detector.

The very dense material  $\text{PbWO}_4$  causes incident photons and electrons to shower. Resulting pair produced electrons and positrons, and radiated photons, cause scintillation light in the transparent, polished crystals. The amount of light produced is proportional to the incident particle energy, and is collected by an Avalanche Photo-Diode (APD) on

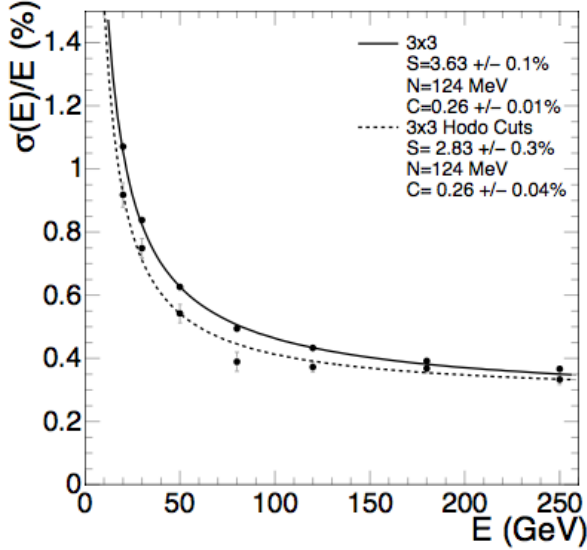


**Figure 3.6:** The energy resolution of an ECAL supercrystal, measured in a test beam. The lower set of points along the dashed line correspond to the energy measured in an array of  $3 \times 3$  crystals, where events fall within a  $4 \times 4$  mm region in the central crystal.

the end of each crystal in the barrel, and a Vacuum Photo-Triode (VPT) in the endcaps. [check if use these acronyms again] These photodetectors also have to be radiation hard and operate successfully in the 3.8 T magnetic field, while providing significant amplification to signal. Both the crystal and photodetector performance has a strong temperature dependence, so the ECAL is kept at a constant temperature of 18° via a water cooling system, and is stable to  $\pm 0.05$  °C.

The energy resolution of the ECAL can be parametrised using the following equation:

$$\left(\frac{\sigma}{E}\right)^2 = \left(\frac{S}{\sqrt{E}}\right)^2 + \left(\frac{N}{E}\right)^2 + C^2, \quad (3.2)$$

where  $S$  is due to stochastic scattering,  $N$  is due to noise and  $C$  is the constant term. Measurements in test beam are shown in Figure 3.6, where the terms were found to be:  $S = 2.8\%$ ,  $N = 0.12$  GeV and  $C = 0.30\%$ .

### 3.2.3 The Hadronic Calorimeter

The HCAL provides complementary energy measurements of hadronic showers, crucial for measuring jets and missing transverse energy. It is a sampling brass calorimeter, built

from alternating layers of large, absorbing brass plates, interleaved with scintillating plastic tiles arranged in trays. Sitting within the bore of the solenoid, the Hadron Barrel (HB) covers pseudorapidity  $|\eta| < 1.3$ , and the Hadron Endcaps (HE) on each side enclose  $1.3 < |\eta| < 3$ . To attain a most hermetic detector, there is also a Hadron Forward (HF), which extends coverage right up to  $|\eta| < 5.2$ .

The quality of the HCAL's measurements is dictated by the fraction of the hadronic shower that passes through the scintillator; the plastic must be thick enough to catch the majority of the shower. This demand for radial extension is at odds with the location of the HCAL, from the outer edge of the ECAL at  $r = 1.77$  m, and the inner edge of the solenoid at  $r = 2.95$  m. Providing a compromise, an outer hadronic calorimeter, Hadron Outer (HO), is placed outside of the vacuum tank of the magnet and supplements the HB. Using the solenoid coil as absorber material, it can identify late starting showers, providing sufficient containment for 11.8 interaction lengths. Five rings of HO are arranged along the  $z$ -axis of the detector, where the central ring at  $\eta = 0$  has two layers at  $r = 3.82$  m and 4.07 m, and the rest have a single layer at  $r = 4.07$  m. Figure 3.7 shows the geometry of the HCAL.

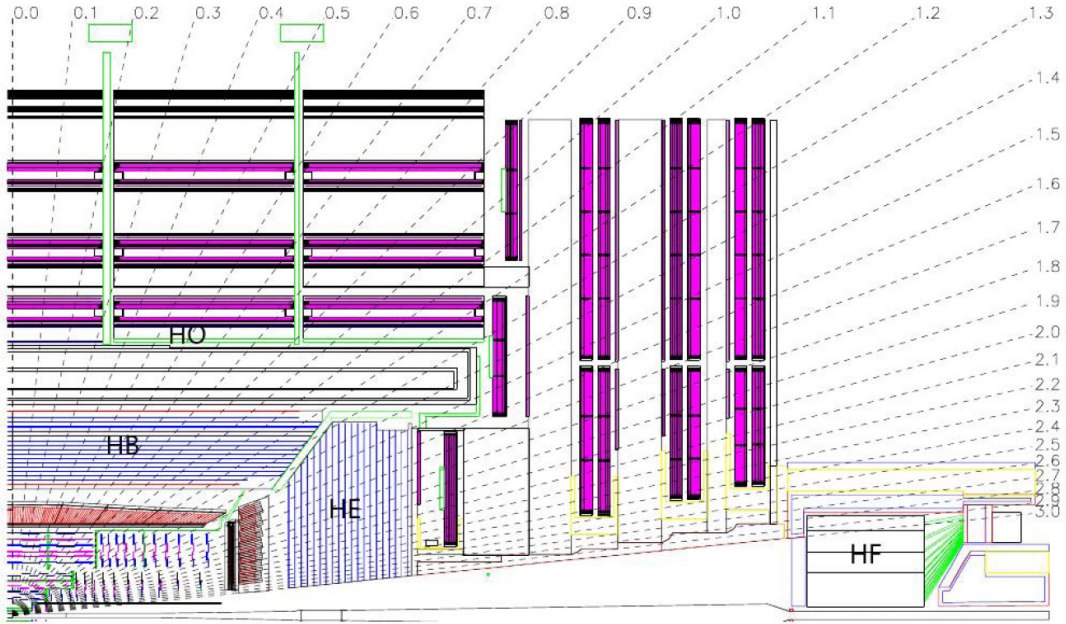


**Figure 3.7:** Longitudinal view of the CMS HCAL. Locations of the HB, HO, HE and HF are shown with values of  $\eta$ . The purple regions represent the muon detectors which further restrict the volume of the HO.

Hadron showers are created in the brass absorber plates, through nuclear interactions in the material, and the plastic scintillator tiles produce blue-violet light when the shower

passes through. It is read out using wavelength shifting fibres, sending the now green light down transparent fibres to Hybrid Photodetectors (HPD) which produce an electrical signal proportional to the incident hadron energy. The first layer of plastic tiles are placed in front of the first absorber plate in order to sample the incoming shower as it develops in the material between the ECAL and the HCAL. The final layer of scintillator placed after the final brass plate to catch any late developing showers. There are 70,000 plastic scintillator tiles in the HB and 20,916 tiles in the HE.

The HF uses a different technology in order to cope with the much harsher environment in which it is situated. With an average energy of 760 GeV deposited in the HF per pp collision at LHC design energy, peaking at the highest rapidity point closest to the beam line, radiation hardness and occupancy requirements demand alternative materials. Steel absorber plates are embedded with scintillating quartz fibres, which act to detect the Cherenkov light emitted by charged particles in the shower. It is therefore most sensitive to the electromagnetic component of the shower.

The energy resolution of the HCAL was measured in pion beam tests. The energy response and resolution are shown in Figure 3.8, and the fractional energy response is parametrised as  $\frac{\sigma}{E} = \frac{120\%}{\sqrt{E}} \oplus 6.9\%$ .

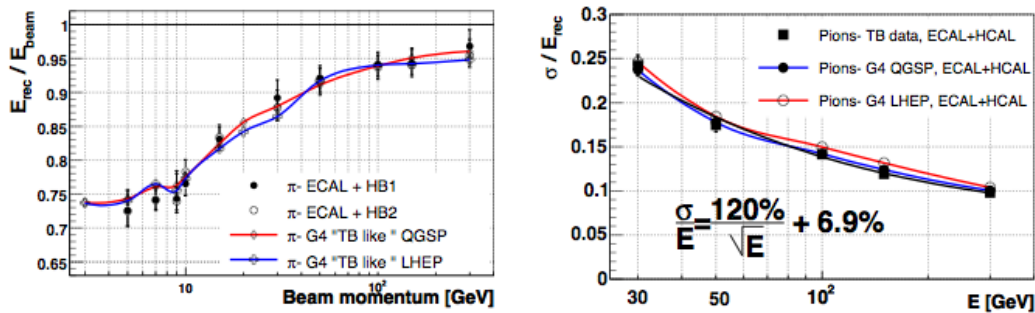


**Figure 3.8:** The raw energy response (left) and fractional energy resolution (right) as a function of energy, for pions, in team beam data.

### 3.2.4 The Muon System

Muons are a powerful tool for recognising signs of interesting physics. A relatively easy experimental signature to identify, muons can provide excellent 2- or 4-particle mass resolutions as, due to their larger mass, they do not suffer large radiative losses (as electrons do). Muon reconstruction is therefore a central design feature. Embedded in

the iron flux-return yoke of the solenoid, the muon system combines three methods of gaseous detection to identify, carry out high resolution momentum measurements, and trigger events, up to  $|\eta| < 2.4$ . Figure 3.9 shows a cross section of one of the five wheels that make up the barrel section of muon system; there are also two planar endcaps which sit at either end of the detector and enclose it.

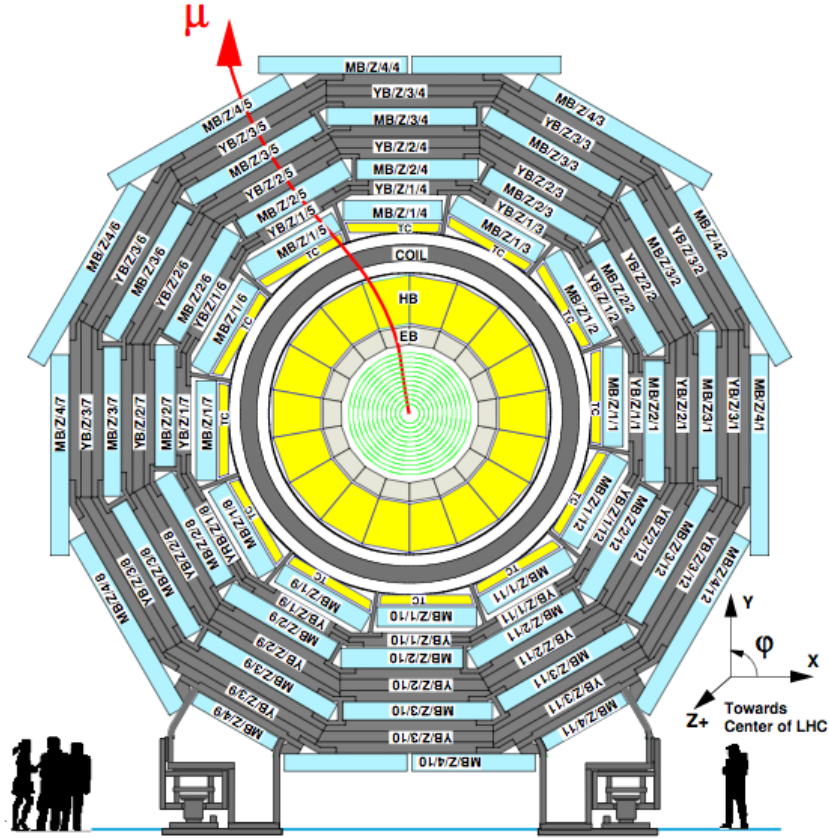


**Figure 3.9:** One of the 5 wheels of the barrel of the CMS muon system. Gaseous detectors are embedded in the iron return yoke of the solenoid; due to the small residual magnetic field in the barrel, DTs are used.

In the barrel ( $|\eta| < 0.9$ ), magnetic flux is concentrated in the iron return yoke so the residual field is very small. There is also a low muon rate and neutron induced background, so DT chambers are used. In the endcaps ( $0.9 < |\eta| < 2.4$ ), magnetic field and muon rate are much higher, so Cathode Stripe Chambers (CSCs) are used instead; they have a faster response time, higher granularity and better radiation hardness. Both the DT and CSCs have excellent position resolution. An additional system of Resistive Plate Chambers (RPCs) in both the barrel and endcaps provide an independent signal which has good time resolution (and poorer position resolution) and serves as a trigger.

By combining information from the tracker, and from either the DT or CSCs and RPCs, CMS has excellent muon reconstruction. Precise momentum resolution is achieved for the kinematic range, from 10 GeV to  $> 500$  GeV, shown in Figure 3.10.

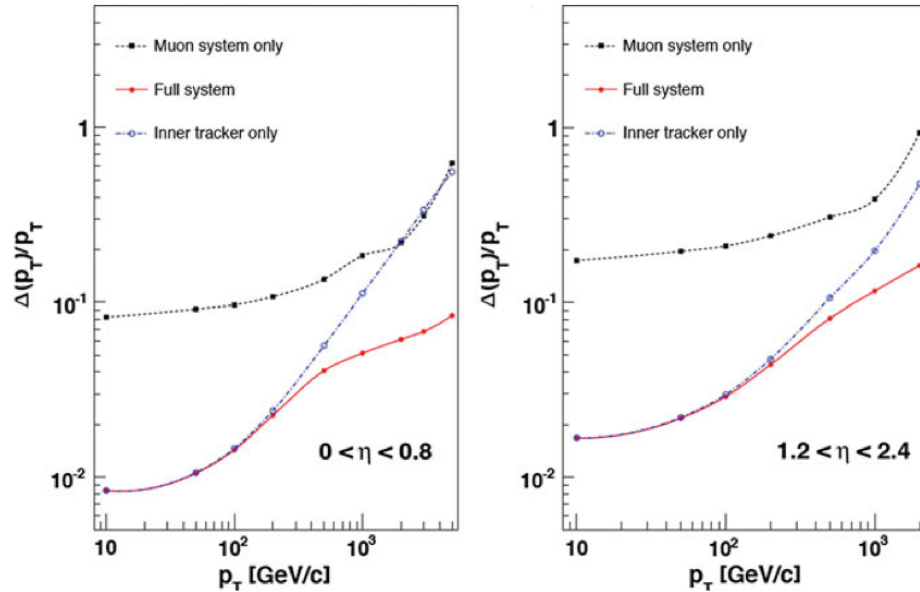


**Figure 3.10:** Muon transverse momentum resolution, shown as a function of muon  $p_T$  in the barrel (left) and the endcaps (right). The resolution of the tracker and muon system is shown, and the enhancement gained by combining the information.

### 3.3 Event Reconstruction

It is by piecing together the information from the various subsystems of the CMS detector that, for example, a track in the tracking system, or an energy deposit in the HCAL, can be attributed to a particle or “physics object”. Figure 3.11 shows a slice of the whole detector with each of the main physics objects traversing it: muons, electrons, photons, and charged and neutral hadrons. Each of these leaves a different signature. Charged particles leave tracks in the silicon tracker, curved under the influence of the magnetic field. Electrons and photons cause electromagnetic showers, leaving energy deposits in the ECAL. Hadrons penetrate further, showering and leaving energy deposits in the HCAL. Muons are the only visible particles to reach the muon system, where they leave tracks.

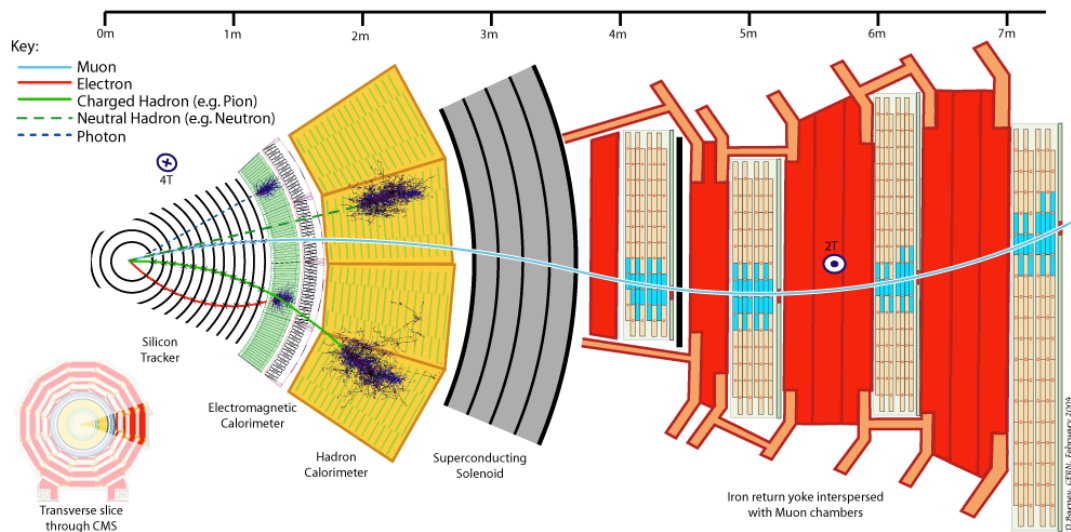


**Figure 3.11:** A slice of the CMS detector is shown, with various particles, or physics objects, traversing it. By combining information from each of the subdetectors, each of the particles produced in an event can be identified and the whole event reconstructed.

Particles can then be identified by combining tracking information with data from the calorimeters and muon system. If there is an energy deposit in the ECAL, the only way to distinguish between a photon or electron is by looking to see if there are hits in the tracker, leading to the position of the electromagnetic shower in the calorimeter. Similarly, the momentum measurement of the electron, determined using the curvature of the track it leaves (also used to reconstruct its charge), can be combined with the energy measurement made using the amount of scintillation light produced in the ECAL to get a better resolution. If there is no track leading to the electromagnetic shower,

a photon is instead reconstructed. Hadronic showers in the HCAL due to charged and neutral incident hadrons can also be distinguished by their tracks. A muon will leave the tell-tale sign of hits in the tracker, and hits in the outer muon chambers, where position, momentum and charge measurements from both ensure the initial track in the silicon tracker matches up to the track in the muon system. Dual measurements also lead to enhanced resolution.

Below is a summary of the object reconstruction most relevant to the physics analysis described in Chapter 5. More information can be found in Ref. [20].

### 3.3.1 Jets

Copious numbers of quarks and gluons are produced during pp collisions in CMS, a consequence of the huge Quantum Chromo-Dynamics (QCD) cross section. Through the strong interaction they fragment and immediately hadronise, and a spray of hadrons is produced in the direction of an initial quark or gluon. Various algorithms have been developed in order to group the spray of hadrons into a “jet”, and assign an energy, direction and transverse momentum to it.

In the analysis presented in this thesis (and in general at CMS), the anti- $k_T$  algorithm [21] is used with a distance parameter,  $R = 0.5$ . It behaves like an idealised cone algorithm, using a distance parameter to cluster particles into cone shapes, with a radius  $R$ . Soft particles are clustered with nearby hard particles rather than with themselves, leading to conical jets, which - crucially - are resilient to soft radiation on the boundary of the cone. Likewise, the area of the jet is unaffected by soft radiation on the boundary, and is equal to  $\pi R^2$ . These features make the anti- $k_T$  algorithm the preferential jet algorithm at CMS, due to its insensitivity to soft radiation that arises from sources such as PU; see Figure 3.12.

Several types of jets exist at CMS, in which the anti- $k_T$  algorithm is given different inputs. Calorimeter (Calo) jets use information from the calorimeter only. ECAL crystals are grouped in  $5 \times 5$  arrays into “towers”, which measure  $0.087 \times 0.87$  in  $\Delta\phi \times \Delta\eta$  space (in the barrel region) and are matched to aligning blocks of HCAL. The sum of the energy deposits in both layers of calorimeter are used as inputs to the jet algorithm, where towers are treated as massless and an  $\eta$  dependent energy threshold has been placed on each tower to reduce the effect of instrumental noise.

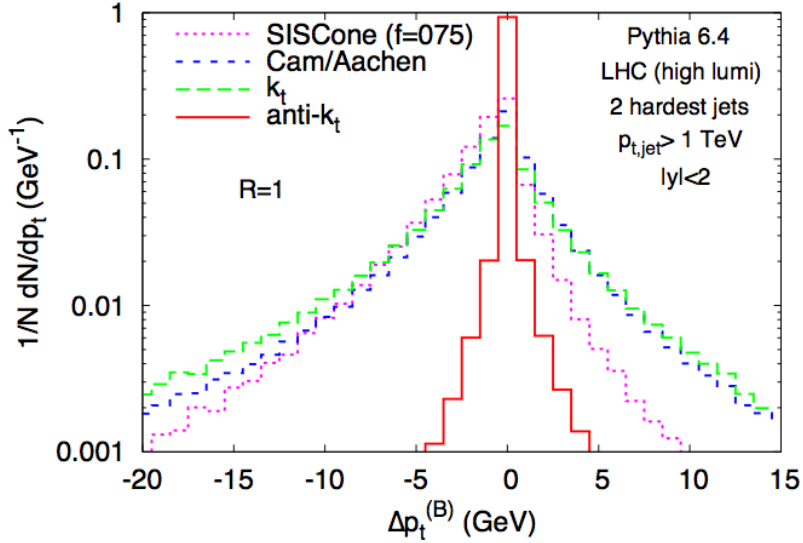


**Figure 3.12:** The relative insensitivity of the anti- $k_T$  algorithm to PU is shown, compared to other common jet algorithms. The distribution of back reaction, corresponding to the net change in  $p_T$  to each of the two hardest jets (where each jet has  $p_T > 200 \text{ GeV}$ ), when adding PU  $\sim 25$  to the event, corresponding to LHC running conditions in the next phase of data taking starting in 2015. Taken from [21].

The Particle Flow (PF) algorithm [22] creates a list of all stable particles in an event: photons, electrons, muons, neutral hadrons and charged hadrons. Particle momentum, direction and type are determined using all of the subdetectors of CMS, which, with its silicon tracker, highly granular ECAL and strong magnetic field is ideally suited to the task. The reconstruction of the fundamental constituents of a typical jet - largely photons, charged hadrons and neutral hadrons - uses charged particle tracks and calorimeter clusters, termed “elements”. A traversing particle is expected to give rise to one, or several elements arising from separate subdetectors. To reconstruct a particle, these elements are therefore grouped into “blocks”: links of one, two or three elements that have arisen due to the same object. Blocks can then be interpreted as individual particles, and the resulting list of reconstructed particle flow particles gives a global description of each event. This list of particles is used as the input to the anti- $k_T$  algorithm, producing PF anti- $k_T$  jets.

The energy of a typical jet consists of energy from charged particles (65%), photons (25%) and neutral hadrons (10%). Therefore, typically, 90% of the jet energy can be reconstructed with good precision, utilising measurements from the high resolution silicon tracker and ECAL. Only 10% of the energy, arising from neutral hadrons, is reconstructed

using the relatively poor resolution hadron calorimeter. Therefore, PF jets, made of reconstructed particles, are much closer to jets made of simulated, Monte Carlo (MC) generated particles than those that rely just on calorimeter information alone (such as Calo jets), see Figure 3.13. PF jets consequently have excellent position and energy resolution. Jet momentum resolution, defined as the ratio  $(p_T^{\text{rec}} - p_T^{\text{gen}})/p_T^{\text{gen}}$ , (where “rec” is for reconstructed, i.e. PF or Calo jets, and “gen” is for jets taken from simulation) is shown in Figure 3.14. It is because of the excellent performance of the PF algorithm, as input to the anti- $k_T$  that it is used most commonly across CMS analyses, including in the analysis presented in this thesis.

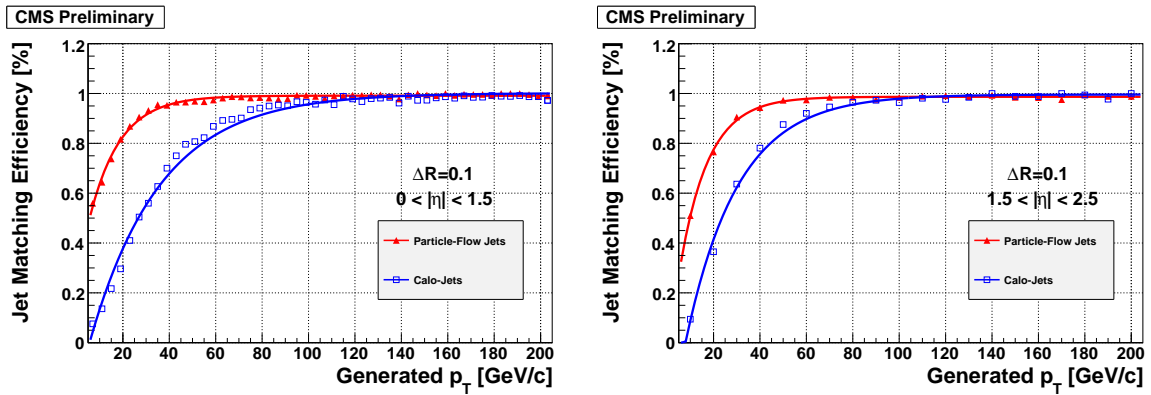


**Figure 3.13:** The efficiency of PF jets, and Calo jets, matched to generated jets in the barrel region (left) and the endcap (right), taken from [22]. The superior performance of PF jets is evident because they are more efficiently matched to the generator, “truth” jets, at a lower  $p_T$  threshold: termed a sharper turn-on.

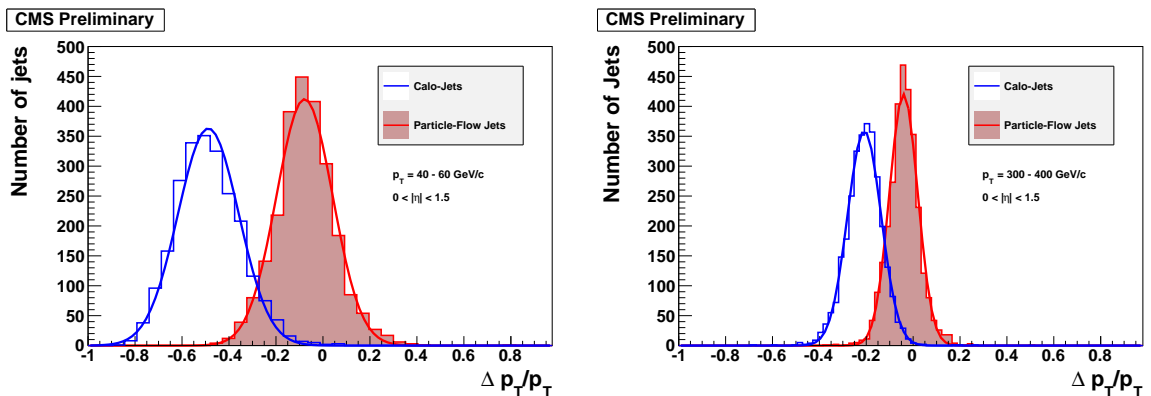


**Figure 3.14:** The momentum resolution,  $(p_T^{\text{rec}} - p_T^{\text{gen}})/p_T^{\text{gen}}$  of PF jets, and Calo jets, for low energy jets ( $40 \text{ GeV} < p_T < 60 \text{ GeV}$ ) (left) and for high momentum jets ( $300 \text{ GeV} < p_T < 400 \text{ GeV}$ ) (right) in the barrel region, taken from [22]. Not only are the peaks sharper for PF jets, meaning a smaller (and therefore better) overall momentum resolution, but it is also peaking much closer to zero, meaning the jet measurement is much closer to the generated jet momentum.

### 3.3.2 Missing Transverse Energy

As discussed in the previous sections, CMS is nearly hermetic, has coverage up to  $|\eta| = 5$  and excellent particle reconstruction; a very complete picture of each event is available. As such, it is very well suited to make measurements of weakly interacting particles, such as neutrinos, that do not leave any trace within any subsystem of the detector; and are only evident through an imbalance of transverse momentum. New physics processes, such as R-parity conserving SUSY, would also lead to signatures involving a large imbalance in transverse momentum as the weakly interacting Lightest Supersymmetric Partner (LSP) exits the detector. DM production would also lead to such a signature. Measurements of missing transverse energy and momentum are therefore crucial to the search for new physics at CMS, as they have been crucial in previous discoveries - for example of the W boson [23], and in searches for other processes [24, 25].

The missing transverse energy vector,  $\vec{E}_T^{\text{miss}}$  is formed by adding the transverse energy vectors  $\sum \vec{E}_T$  of all the particles formed in an event. The missing transverse energy vector  $\vec{E}_T^{\text{miss}} = -\sum \vec{E}_T$ , where  $|\vec{E}_T^{\text{miss}}| = E_T^{\text{miss}} = |\sum \vec{E}_T|$ ; i.e., it is equal in magnitude and opposite in direction to the total visible energy in the event. In an analogous way to jets (and usually using such jets),  $E_T^{\text{miss}}$  can be built using various algorithms. Calorimeter (Calo)  $E_T^{\text{miss}}$ , in the same way as Calo jets, is built from calorimeter information alone while PF  $E_T^{\text{miss}}$  is calculated from all of the transverse energies of reconstructed particles in an event. In a similar way to the jet algorithms, a better resolution is achieved using the PF algorithm over calorimeter information alone, see Figure 3.15. However, because energy measurements of particle flow objects are driven by calorimeter resolution, particularly for large  $E_T$  objects, the improvement is less marked. In the analysis presented in this thesis, PF  $E_T^{\text{miss}}$  is used, where any muons present have been removed from the calculation. It therefore mimics Calo  $E_T^{\text{miss}}$ , only with an enhanced resolution.

### 3.3.3 Muons

Muons are reconstructed using the muon systems and the tracker, and the reconstruction algorithms use the concept of “regional reconstruction”. On the basis of an input or seed from the muon systems, the software only reconstructs the part of the tracker from which the muon causing the seed could originate. This means that only a very small part (typically a few percent) of the tracker volume must be processed to reconstruct a muon;

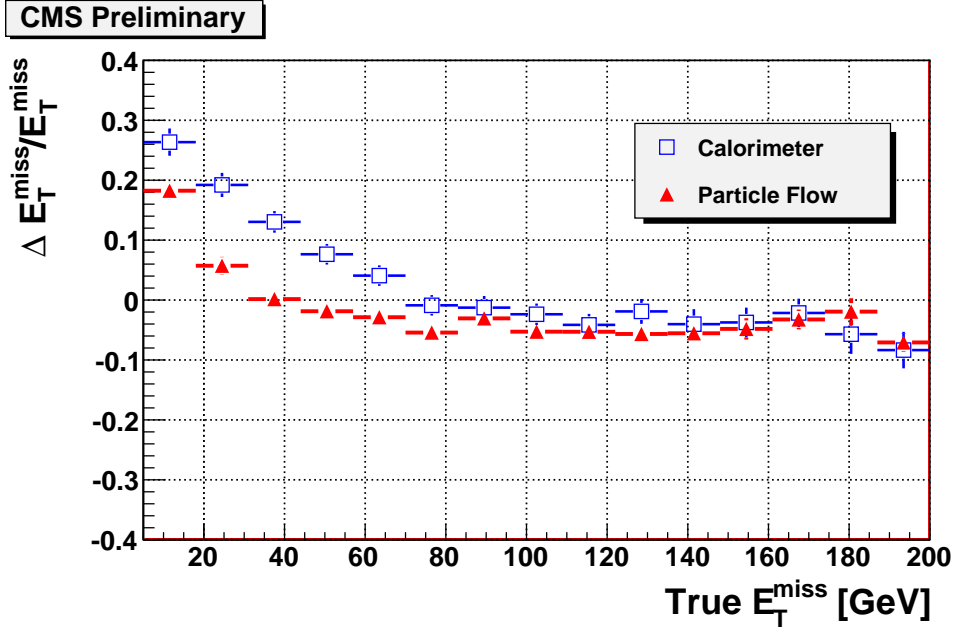


**Figure 3.15:** The momentum resolution,  $(E_{T,\text{rec}}^{\text{miss}} - E_{T,\text{gen}}^{\text{miss}})/E_{T,\text{gen}}^{\text{miss}}$ , of PF and Calo  $E_T^{\text{miss}}$ , taken from [22]. An improved resolution is seen using the PF algorithm, particularly at low values of  $E_T^{\text{miss}}$ . At higher  $E_T^{\text{miss}}$  values, energy measurements are dominated by the calorimeter resolution and values using the two different methods converge.

thereby speeding up the procedure and reducing the CPU power necessary to process an event.

Muon reconstruction has three stages: local, standalone and global reconstruction. Starting with a seed which defines a region of interest, which could be from the Level 1 Trigger (L1) Trigger seeds (from the RPCs) or from patterns of hits found in the CSCs and/or DT, a local reconstruction is performed in surrounding compatible muon chambers. The standalone reconstruction uses information from just the muon system; measurements of track position, momentum and direction of travel are taken, and extrapolated to the nominal interaction point. Global reconstruction then extends the resulting muon trajectories to include hits in the silicon tracker. A track is extrapolated from the innermost muon chamber to the outer tracker surface, and compatible silicon layers determined. Candidates for the muon trajectory are built from pairs of hits in separate layers of the tracker and  $\chi^2$  of the fit is used to ensure a “good” muon candidate; to detect any bremsstrahlung or significant energy loss. High energy muons present particular difficulty as they suffer huge energy loss and severe electromagnetic showers in the muon system; the  $\chi^2$  probability of the fit compared to the the  $\chi^2$  probability of the tracker only trajectory allows accurate momentum reconstruction of such objects.

### 3.4 The Trigger

The pp interaction cross section is 100 mb, while for example, the W boson production cross section is some 6 orders of magnitude less than this, and the rare physics processes that CMS was built to search for, such as Higgs boson and SUSY production, many times smaller still; see Figure 3.16. The LHC delivers an unprecedentedly high instantaneous luminosity so that such rare physics processes occur, but this also implies that the vast majority of the collisions result in ‘uninteresting’ physics: namely relatively low energy, soft scattering events. It would be impossible to record the very high volumes of data that come out of CMS, some PB s<sup>-1</sup>, and not useful to do so. Therefore, a very efficient method of recording those events that appear ‘interesting’ is necessary.

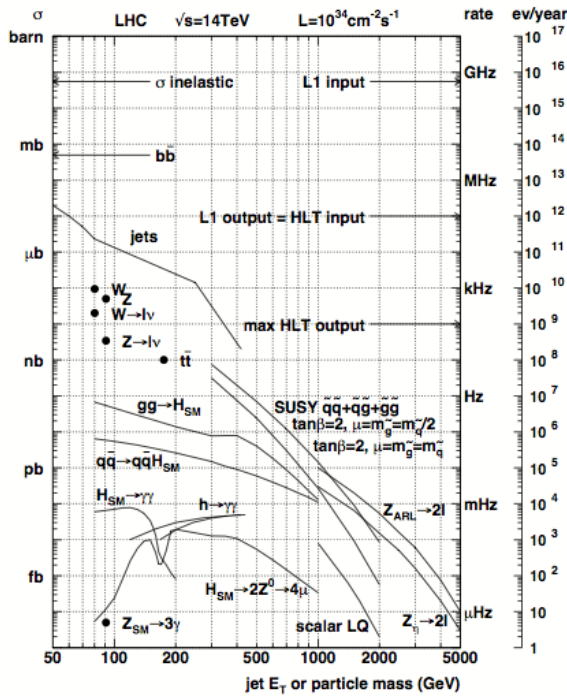


**Figure 3.16:** Inclusive pp cross sections ( $\sigma$ ) for basic and rarer physics processes, showing some of the phenomena on the physics programme at CMS. Shown on the right are the interaction rates for LHC design luminosity,  $10^{34}\text{cm}^{-2}\text{s}^{-1}$ . Taken from [26].

A two tier trigger system reduces the 40 MHz LHC bunch crossing rate to an output of 100 Hz, which is then saved offline to be reconstructed ready for physics analysis. The hardware based L1 uses fast algorithms with coarse inputs from the calorimeter and muon system to efficiently select, online (that is at the same rate as LHC bunch crossings), those events that appear interesting, reducing the 40 MHz collision rate to

100 kHz. A software based Higher Level Trigger (HLT) running on the event filter PC farm at Point 5 takes the output of the L1 trigger and reduces it further to 100 Hz, using more sophisticated inputs and algorithms. Performance of the subdetectors and readiness to collect data, monitored by the Data Acquisition System (DAQ) system, is supervised by the trigger control system. Events passing HLT selection requirements are sent to the CERN Computing Centre where complex algorithms using all the information from the CMS detector are used to fully reconstruct the event. More information on the CMS trigger can be found in Ref. [26].

### 3.4.1 The L1 Trigger

Low granularity inputs from the calorimeter and muon system are used to quickly select possibly interesting events, based on predefined and programmable algorithms and criteria. Parts of the hardware are Field Programmable Gate Array (FPGA) based, allowing some flexibility in algorithms, while other parts are Application Specific Integrated Circuit (ASIC) based, with predefined criteria. Events are selected if they show signs of interesting physics; for example have jets, electrons/photons, or muons. Global quantities such as total transverse energy and total missing transverse energy are also used. In order to see if an event contains any of these physics objects above a pre-defined energy threshold or multiplicity, the L1 trigger is separated into the Calorimeter Trigger, which looks for jets, photons and electrons, and the Muon Trigger, which looks for muons. Global quantities are computed at the Global Trigger (GT) and combined with information from the Calorimeter and Muon triggers, and here a decision is made to keep or reject an event.

In the Calorimeter Trigger, information from the ECAL, HCAL and HF are combined. First, the calorimeter is split into different (geographical) regions, and electron, photon and jet finding algorithms run on the separate parts of the subdetectors at the Regional Calorimeter Trigger (RCT). Information from the different regions is then combined at the Global Calorimeter Trigger (GCT). In the Muon Trigger, information from the DT, CSCs and RPCs are combined. Muon track finding algorithms are applied to data from the DT and CSCs at the Regional Muon Trigger (RMT), and the Global Muon Trigger (GMT) combines information from all of the three subdetectors to get an enhanced resolution. Inputs from the GCT and GMT are then combined at the GT, where the decision to keep or discard an event is made. The architecture of the L1 trigger is shown in Figure 3.17.

There is an inbuilt latency of  $3.2 \mu\text{s}$  in the L1 trigger, meaning that on the first bunch crossing, it takes up to  $3.2 \mu\text{s}$  to transmit the necessary information, and make a decision. This is driven by the data storage available for information from the tracker and preshower detectors; they need so much data storage that it must be saved before a L1 accept decision, and subsequent event read out, can be made. The decisions on the rest of the bunch crossings follow at the rate of collisions, and the architecture is ready to accept another event every 25 ns.

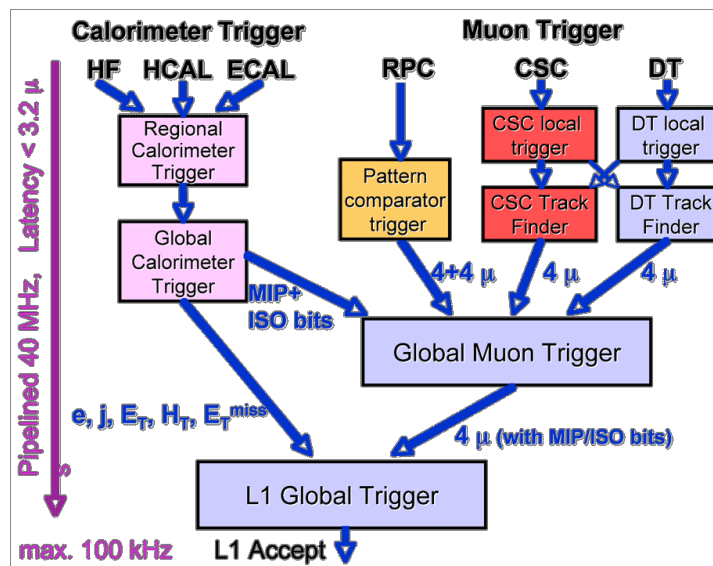


**Figure 3.17:** Architecture of the L1 trigger. The calorimeter trigger takes inputs from the ECAL, HCAL and HF. The muon trigger takes inputs from the DT, CSCs and RPCs. A decision is made at the L1 GT, using inputs from the GCT and the GMT, of whether to pass an event onto the HLT or discard it.

A L1 accept decision is based upon the results of the various physics object reconstruction algorithms. Typically, every physics analysis has a type of event it is searching for; a particular topology. For example, the monojet analysis looks for events with a final state of one high  $p_T$  jet and large missing transverse energy. At L1, it requires the global variable of an event, total missing transverse energy, above 36, 40 or 50 in L1 units of energy. A L1 trigger menu, comprised of all of the required L1 seeds for the whole physics programme at CMS, gives a certain bandwidth to each of the seeds. A low threshold seed will typically demand a large amount of bandwidth as more events are likely to be lower in energy, whereas a high threshold will require a lower bandwidth. Combined, the output to the HLT of all of the L1 seeds in the trigger menu must not exceed the design rate of 100 kHz.

### 3.4.2 The High Level Trigger

When an event is accepted by the L1 trigger, the full detector information for that event (consisting of around 1 MB of data) is passed onto the HLT. On the event filter farm, which consists of over 1000 PC's, all of the detector information for each event is processed. Information not available at L1 becomes available. The additional computing power and longer time scales mean the full granularity of the calorimeter and tracker information (as well as L1 objects), can be used as inputs to more complex algorithms. As a result, much more stringent requirements are used to select events of interest, creating datasets which are used for offline analysis.

An analysis will typically use more than one HLT trigger, and similarly more than one analysis might use the same trigger (and an event pass more than one trigger). For example, the monojet analysis uses a combination of three triggers which demand large missing transverse energy in every event, or a single high momentum jet in addition to large missing transverse energy. This allows events with a monojet topology to be selected efficiently; further kinematic and topological selections are applied offline to a dataset formed of events passing these trigger requirements. Similarly, every physics analysis uses a trigger (or triggers) suited to the topology under investigation.

In the same way that there is a L1 trigger menu, there is also a HLT menu comprised of all of the HLT trigger paths, and the bandwidths they require, which meets the needs of all of the physics analyses at CMS. The total bandwidth of the HLT menu must not exceed 100 Hz or 100 events saved offline per second, limited by the resources necessary to process and store events; namely Computer Processing Unit (CPU)s and disk space available.

# Chapter 4

## Jet Algorithms for the L1 Trigger Upgrade

In the hadron rich environment of the LHC, the hadronisation of quarks and gluons into jets is a major component of the physics programme of CMS. Whether for standard model analyses, Higgs searches, SUSY searches or exotic analyses, jet reconstruction is vital for both event selection and offline analysis, for a wide range of jet kinematic requirements. Efficient and reliable triggering on jets is therefore of key importance and the first stage of event selection, the L1 trigger, must have an effective jet algorithm. This is of particular significance as we look towards the LHC upgrade, when running conditions become increasingly challenging. Up to double the instantaneous luminosity and centre-of-mass energy lead to an increase of PU up to  $\sim 70$  and far higher detector occupancies. Jet algorithms must maintain a similar performance in this next phase of LHC running as exhibited in the previous period of data collection. A new L1 jet algorithm is proposed, which exploits the full granularity of the calorimeter and uses event-by-event PU subtraction.

### 4.1 The LHC Upgrade

Following the tremendously successful operation during Run I in 2010-2012, where the CMS and ATLAS experiments collected around  $5 \text{ fb}^{-1}$  at 7 TeV and  $20 \text{ fb}^{-1}$  at 8 TeV, the LHC is currently in a period of shut-down, termed “Long Shutdown 1” (LS1). Magnet interconnections are being replaced and the dipole magnets are undergoing a quench training programme. These improvements to the LHC magnets will allow safe acceleration

of protons up to 7 TeV in each beam, and sustained operation at  $\sqrt{s} = 13$  TeV, eventually to achieve the design energy of 14 TeV. This will nearly double the available centre-of-mass energy as compared to Run I, potentially making Run II a discovery run - opening up more phase space and therefore opportunities for finding new physics. Instantaneous luminosity will also increase, with the aim of providing the number of events to give the statistical precision required to search for the rarest processes, as well as shed more light on the properties of the boson discovered during Run 1 [8, 9, 27]. After a period of a year or so of running after LS1 termed “Run II”, the LHC will again undergo a period of shutdown, “Long Shutdown 2” (LS2), in which improvements to the accelerator injector chain will be made - with the aim of providing much greater instantaneous luminosities. The potential luminosity performance of two scenarios for future running of the LHC is shown in Table 6.1.

Scenario	# bunches	$\mathcal{L}$ ( $\text{cm}^{-2}\text{s}^{-1}$ )	Pile-up	$\text{L}$ ( $\text{fb}^{-1}/\text{year}$ )
25 ns	2760	$9.2 \times 10^{33}$	21	24
50 ns	1260	$2.2 \times 10^{34}$	40-76	45

**Table 4.1:** Two of the possible luminosity performances for LHC running during Run II, taken from [28].

If the machine operates at 50 ns, the instantaneous luminosity will double compared to that of Run I, with PU expected to more than double from around 20 inelastic collisions per bunch crossing to in excess of 70. Not only will the number of interactions per second increase due to the higher instantaneous luminosity, but the increased centre-of-mass energy means the energy of these interactions will also increase. Consequently, for a particular trigger (say, for example a single jet trigger), many, many more events will pass a particular energy threshold as compared to Run I. As a result, the trigger rate will soar.

For a single jet trigger, where the jet (reconstructed offline) is required to be above 128 GeV, 95% of jets which have been matched to this offline jet and reconstructed using the existing L1 jet algorithm are above 150 GeV- where the higher L1 threshold is due to poorer L1 reconstruction than offline reconstruction. In a typical run during 2012 (PU=15,  $\mathcal{L} = 0.4 \times 10^{34} \text{ cm}^{-2}\text{s}^{-1}$ ), a L1 jet threshold of 150 GeV corresponds to a rate of 1.1 kHz. In the high PU test runs during 2012 that had a few bunches filled which could then be scaled up to high luminosity and PU, this trigger rate rose to 3.6 kHz (PU=45,  $\mathcal{L} = 1.1 \times 10^{34} \text{ cm}^{-2}\text{s}^{-1}$  equivalent); and simulation shows that in similar conditions but

at 14 TeV, a trigger rate of 14 kHz is expected. The total rate of all of the L1 triggers is capped at 100 kHz by design, and a balanced trigger menu is desirable to satisfy all of the physics demands of CMS. Therefore, individual trigger rates must be kept reasonably low to ensure the total L1 trigger rate is acceptable. The only way to maintain low trigger rates in the more challenging run conditions is to increase energy thresholds. Figure 4.1 shows an illustrative L1 trigger menu for the upgraded LHC, for bunch spacings of 25 and 50 ns. Thresholds have had to be significantly raised to maintain a total rate below 100 kHz; for example, the single jet threshold is increased to 170 GeV and 205 GeV for 50 and 25 ns bunch crossings respectively.

Trigger Algorithm	Current Level-1 $L = 1.1 \times 10^{34} \text{ cm}^{-2}\text{s}^{-1}$			Current Level-1 $L = 2.2 \times 10^{34} \text{ cm}^{-2}\text{s}^{-1}$		
	Rate [kHz]	95% Threshold [GeV]	Plateau Efficiency	Rate [kHz]	95% Threshold [GeV]	Plateau Efficiency
Single e/ $\gamma$	12	46	1.0	10	67	1.0
Single iso e/ $\gamma$	10	38	0.9	9.4	52	0.9
Single Mu	12	23	0.95	11	42	0.95
Single isoTau	10	65	0.3	9.2	72	0.3
iso e/ $\gamma$ + e/ $\gamma$	10	24 15	0.9	16	26 16	0.9
Mu + Mu	6.3	18 10	0.9	7.4	20 12	0.9
Tau + Tau	7.5	36 36	0.1	8.2	36 36	0.1
iso e/ $\gamma$ + Mu	9.6	21 11	0.85	6.2	24 12	0.85
Mu + e/ $\gamma$	3.3	18 14	0.95	5.0	20 15	0.95
Single Jet	6.4	170	1.0	5.4	205	1.0
Double Jet	4.6	140 140	1.0	5.8	170 170	1.0
Quad Jet	9.4	4@71	1.0	4.8	4@96	1.0
Single iso e/ $\gamma$ + Jet	7.5	32 68	0.9	8.5	38 82	0.9
Single Mu + Jet	8.6	22 43	0.95	7.5	27 54	0.95
Single iso e/ $\gamma$ + $H_T^{\text{miss}}$	10	29 110	0.9	8.2	38 120	0.9
Single Mu + $H_T^{\text{miss}}$	4.6	18 89	0.95	9.8	20 93	0.95
$H_T$	3.9	500	1.0	5.4	580	1.0
Total Rate	94			92		

**Figure 4.1:** The projected L1 trigger menu using the current L1 system and algorithms, at 14 TeV, for illustration purposes. In the left hand column, all of the different triggers contributing to the menu are shown. In the centre (right-hand) columns, the projected L1 trigger rate, 95% threshold and plateau efficiency are shown for running conditions with bunch spacing of 50 ns,  $\mathcal{L} = 1.1 \times 10^{34} \text{ cm}^{-2}\text{s}^{-1}$ , PU=50 (25 ns,  $\mathcal{L} = 2.2 \times 10^{34} \text{ cm}^{-2}\text{s}^{-1}$ , PU=50), taken from [28].

For the physics requirements of CMS the necessary increase in L1 thresholds, and corresponding increase in offline (analysis) thresholds, is an unacceptable compromise as lower energy final states are crucial to many analyses and keeping as much physics,

at as low thresholds as possible, is desirable. To cope with the challenges of the LHC upgrades, and to enable new algorithms (with better performance) to be developed so the physics performance of Run I can be maintained, or bettered, the CMS L1 trigger is also undergoing upgrades.

## 4.2 CMS Trigger Upgrade

Upgrades to the electronics of the calorimeter trigger, muon trigger and global trigger are under way in order to meet the triggering demands of CMS. These upgrades involve installing additional interconnections between the systems, reducing the current huge diversity of electronics cards to a small number of multi-purpose and adaptable cards, using high bandwidth optical links and modern, high powered FPGA processing chips. These upgrades not only allow more information from the detector subsystems to be used as inputs to improved (more sophisticated) algorithms, due to increased logic resources and fast links, but crucially also allow far more flexibility in the L1 trigger system. In Run I, the ability to adapt the trigger algorithms and menu to evolving LHC run conditions proved vital in reducing trigger rates and improving efficiencies. Increasing the flexibility by making more of the system adaptable, and more of the cards standardised, will only improve the trigger and enhance its longevity. Having the ability to easily update software and firmware, as well as trigger architecture, in response to unforeseen circumstances - not just in the planned LHC upgrades to 2016 but far beyond - will put CMS in an excellent position for data collection.

The new L1 trigger is being installed during LS1, and will be commissioned and run concurrently with the existing trigger during Run II. The upgraded system will be available for physics in 2016. Here, I discuss in detail the calorimeter trigger upgrade, as this is what the proposed jet algorithm, detailed in this chapter, relies upon. More information on the muon trigger and global trigger upgrade can be found in [28].

### 4.2.1 Calorimeter Trigger Upgrade

The calorimeter trigger uses information from the ECAL and HCAL to look for electrons/photons and jets, as described in the previous chapter. It currently is based upon a traditional trigger design; where the detector is spatially segmented into different processing nodes, each of which deals with the data from each geographical region, and

does so at every bunch crossing. The desire for far more flexibility in triggering motivates a new approach to the upgrade trigger architecture, known as time-multiplexing. Instead of splitting the detector into geographical regions and sending the data to different processors at every bunch crossing, a Time-Multiplexed Trigger (TMT) places all of the data from the detector in a single processor across several bunch crossings. No data is thrown away at any stage of the process, and all of the data, at its full granularity, is available in the same card making many more algorithms possible.

## Traditional Trigger Architecture

A conventional trigger architecture is shown in Figure 4.2. The calorimeter is split into geographical regions in  $\eta - \phi$ , and at every bunch crossing data from the individual regions are sent to different processors. Boundaries between these regions must be duplicated in each implicated processor, to ensure that any objects found along the boundary are sufficiently dealt with. To achieve a compact implementation, at each stage of the trigger process the volume of data is reduced and the minimal information with which to make a decision is passed onto the GT. Therefore, a lot of the information from an event is discarded before a decision at the GT is made. In addition, the current calorimeter trigger does not use the full granularity of information available, and the combined ASIC and FPGA hardware, although permitting some flexibility in algorithms and parameters, is restricted by a fixed data flow. Not all algorithms can therefore be implemented, and the coarse inputs limit the possible performance.

Energy clusters are built into physics objects with which the GT can make a decision over two processing layers. Trigger towers, consisting of groups of  $5 \times 5$  crystals in the ECAL, and the corresponding blocks of the HCAL, are themselves grouped into  $4 \times 4$  arrays or “regions”. These regions are used as inputs to the various object algorithms. In the first layer, the ‘Regional stages’ in Figure 4.2, the regions, or clusters of transverse energy are assigned a type; electron/photon-like, if energy is predominantly in the ECAL, otherwise hadron-like. In the second processing layer, the ‘Global Stages’, the cluster type is identified as an electron/photon or tau (for high energy or isolated deposits respectively), and non-isolated clusters are grouped together to form jets. The jet finding algorithm looks for energy deposits in windows of  $3 \times 3$  regions, with the requirement that the central region has a larger transverse energy deposit. The top four candidates are passed onto the global trigger, with the rest discarded. Also in this layer of processing, the value and direction of total missing transverse energy are calculated from the sum of

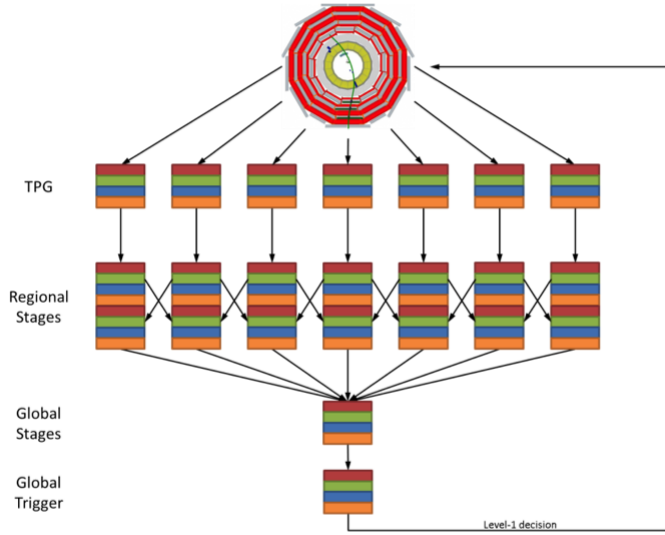


**Figure 4.2:** Conventional trigger architecture, showing data processing in regions. Taken from [?].

energy deposits across the calorimeter, and jet candidates above threshold are summed to give the total hadronic energy content, known as  $H_T$ .

### Time Multiplexed Trigger

A time-multiplexed trigger architecture is shown in Figure 4.3. In a similar way as the HLT, it will consist of parallel nodes, each of which process individual events concurrently. All of the data from an event - from the whole  $\eta - \phi$  range of the calorimeter and at full granularity - are sent to an individual processor. The first processor receives the data from the first bunch crossing over  $N$  clock cycles (where the length of a clock cycle is equal to the time between bunch crossings, 25 or 50 ns). The data from the second bunch crossing are sent to the second processor, again over  $N$  clock cycles, and so on; where there are more than  $N$  processors in total, as each processor needs time to process each event. After the first processor has processed all of the data from the first bunch crossing and passed it on to the next stage of the trigger, the ‘Demux’ in Figure 4.3 (some  $N + X$  clock cycles after the first bunch crossing where  $X$  is the time taken to process and send on the data), it can then receive data from another bunch crossing. Developments in large FPGA chips and increased rate and volume of data transmission in optical fibres make this kind of architecture possible for the upgraded CMS calorimeter L1 trigger, whereas it was not when the current trigger was designed and built. The system latency,  $N + X$ , is now small enough, due to the increased processing power and bandwidths,

that it is viable in hardware for the huge amounts of data and short time-scale that the trigger demands [29].

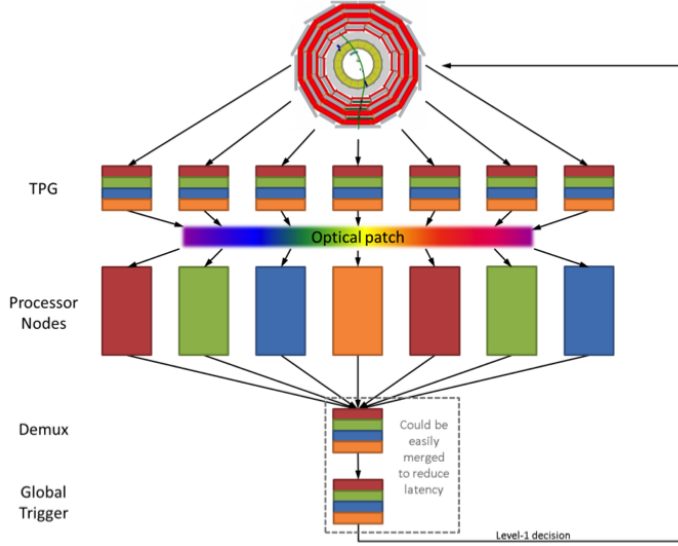


**Figure 4.3:** Time-multiplexed trigger architecture, showing data pipelining to different processing nodes. Taken from [?].

With all of the data, at full granularity, in one single processor, many more algorithms for object reconstruction are possible. Tower level calorimeter inputs (rather than region level inputs) will be available, increasing the granularity by a factor  $4^2$ , with similarly improved spatial resolutions. There is also scope for an array of additional variables, using information from the whole calorimeter. For example, the average energy deposit for each row in  $|\eta|$  or ring of  $\phi$  can be calculated, and used to give an estimate of PU on an event-by-event basis. In the remainder of this chapter, a jet algorithm is proposed for the upgraded L1 calorimeter trigger. More detail on the CMS L1 calorimeter trigger upgrade can be found in Ref. [30].

## 4.3 Algorithm for jet reconstruction at L1

A jet algorithm to reconstruct, filter and calibrate L1 jets is proposed, for the upgraded CMS calorimeter trigger. It is assumed that all of the L1 calorimetric information for a single event streams through a single processor; that is, all of the information from a single bunch crossing can be processed in one single chip. This is compatible with the TMT architecture which will be available after LS2 at CMS.

Using tower level information, the algorithm creates a tunable sized jet at each site on the calorimeter, filters out zero-energy jets and repeats, to get the ‘best’ 13 jet candidates per event. The average jet energy density for each event is calculated, and subtracted from the energy deposited across the calorimeter in order to perform PU subtraction on an event-by-event basis. The 13 jet candidates are then calibrated to offline energy. This algorithm is compared to the current L1 jet algorithm. A much improved spatial resolution is seen, as well as enhanced, and crucially, more PU independent energy resolution. The resulting trigger turn-on curves for various jet energy thresholds, and trigger rates for single and multijet triggers are improved compared to the current algorithm, as well as the global variable  $H_T$ . This jet algorithm was the proposed jet algorithm in the CMS L1 Trigger Upgrade Technical Design Review, Ref. [28].

### 4.3.1 Jet Reconstruction

The proposed jet algorithm uses the full granularity of the calorimeters available at L1; that is,  $5 \times 5$  ECAL crystals grouped together into towers, with the corresponding block of HCAL. In the centre of CMS, each tower measures  $0.087 \times 0.087$  in the  $\eta - \phi$  plane, with the  $\eta$  dimension increasing as  $\eta$  increases; see Figure 4.4. In total there are 72 towers in the  $\phi$  direction, and for  $|\eta| \leq 3.0$  (the barrel region), 56 towers in the  $\eta$  direction. The sum of energy deposits in both the ECAL and HCAL at each tower is used as input to the algorithm.

A group of  $n \times n$  towers is combined to form a jet candidate, where the energy of that jet candidate is the sum of the  $n \times n$  towers it consists of. The jet size,  $n$ , is completely flexible, as well as the jet shape. Jet sizes of  $8 \times 8$  to  $12 \times 12$  were studied, and both circular and square jets. This compares with the current L1 jet algorithm, which consists of equivalent  $12 \times 12$  square jets - where the towers are incorporated into regions, each measuring  $4 \times 4$  towers; see Figure 4.5 for a comparison of the current and proposed upgrade jet geometry. For circular jets the size  $n$  represents the length of the diameter, for square jets it represents the length of the side.

A candidate is created at each individual tower, using a “sliding window” approach. Only jet candidates with non-zero energies are passed onto the next stage, however there remains a huge jet multiplicity at this first stage of jet creation. There is a jet for every non-zero tower, and a huge number of overlapping jets as each tower contributes to  $n^2$  different jets, or, equivalently, each jet candidate has  $(2n - 1)^2$  overlapping jets. Figure 4.6 shows some of jet candidates which overlap, shown in red, with a single jet

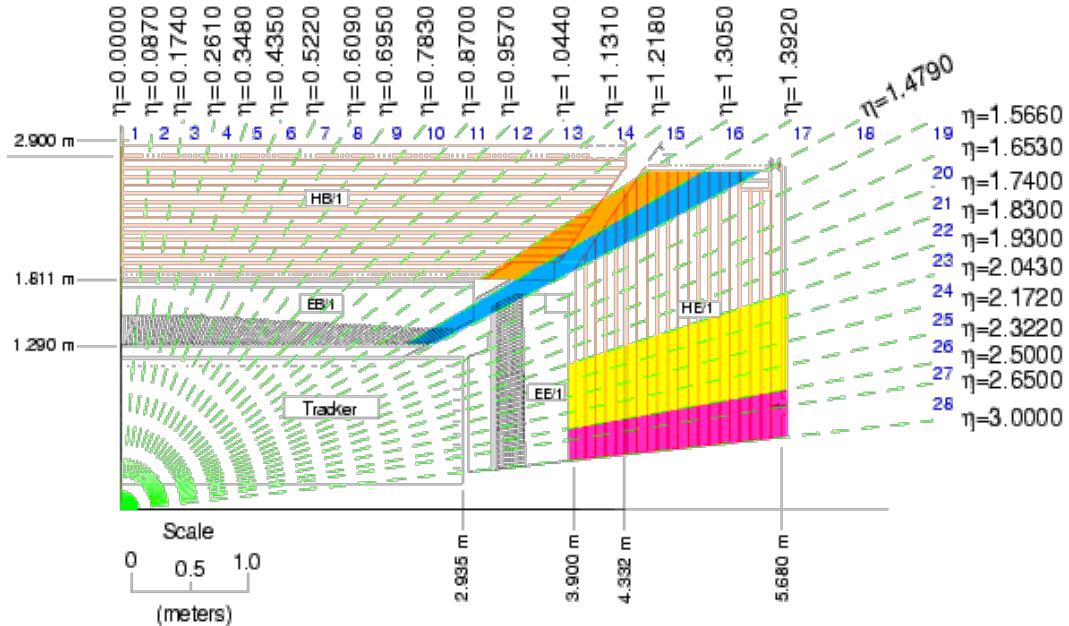


**Figure 4.4:** Layout of trigger towers in the  $r - z$  projection, for  $0 < \eta < 3.0$ . Both ECAL and HCAL towers are shown.

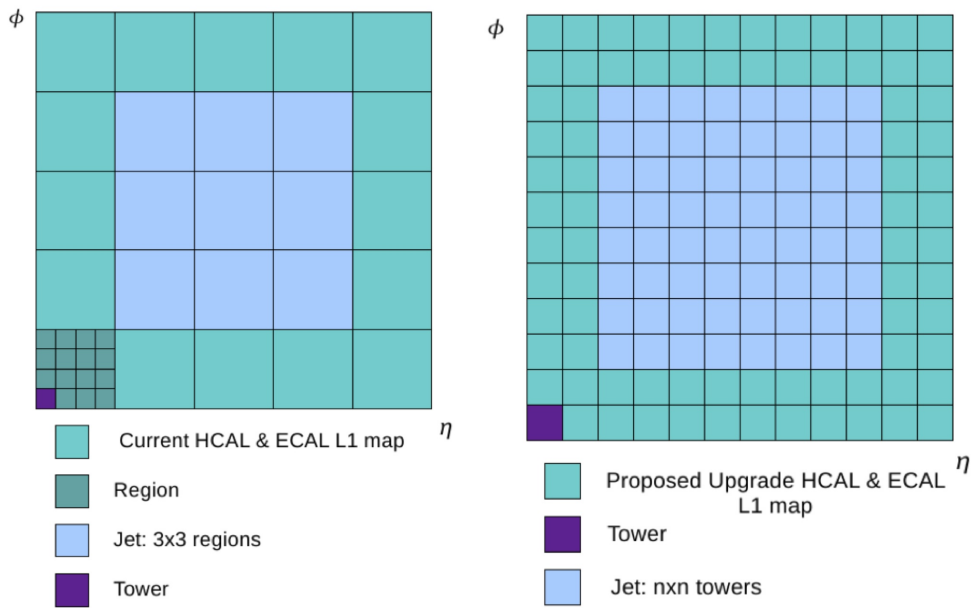


**Figure 4.5:** Comparison of the current L1 jet map, left, with the proposed upgrade jet map, showing a  $8 \times 8$  square jet, right.

candidate measuring  $4 \times 4$  towers and square in shape, shown in purple. The window of all overlapping candidates is shown in blue; and measures  $10 \times 10$  towers. The resulting

numerous overlapping jets must be sorted and filtered to find the highest energy jet of the candidates.

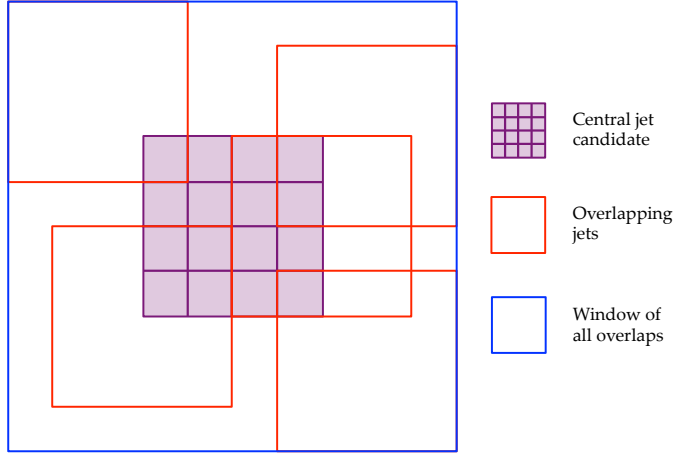


**Figure 4.6:** A few of the overlapping jets of one  $4 \times 4$  jet (centre, purple), are shown in red. The window of all of the jet overlaps is shown in blue, measuring  $10 \times 10$ . These overlapping jets must be sorted and filtered to keep only the most energetic jet.

To give the best angular resolution, the  $\eta$  and  $\phi$  coordinates of the jets are energy weighted,

$$\eta_{jet} = \frac{\sum \eta_{tower} \cdot E_{tower}}{\sum E_{tower}} \quad (4.1)$$

$$\phi_{jet} = \frac{\sum \phi_{tower} \cdot E_{tower}}{\sum E_{tower}}. \quad (4.2)$$

Here, the sum is over all of the towers in a jet window and  $\eta_{tower}$ ,  $\phi_{tower}$  are the coordinates of the individual towers within a jet,  $E_{tower}$  is the transverse energy deposit in the tower and  $\eta_{jet}$ ,  $\phi_{jet}$  are the coordinates of the jet.

In previous studies diameter 8 circular jets gave the best angular resolution, so these are presented here. [Remake plots and include here](#)

### 4.3.2 Jet Filtering

The jet collection must be sorted and filtered to remove the numerous overlaps. Firstly, all jets in each event are ordered in energy using a bitonic sort. This is a recursive parallel sorting algorithm suitable for implementation in hardware. It takes  $2^N$  inputs and sorts in  $N$  steps using a series of bitonic sequences and splits.

However, there is often more than one overlapping jet of a particular energy. An asymmetry parameter in  $\eta$  and  $\phi$  is also considered for each jet when this is the case:

$$A_{\eta,\phi} = \sum (\text{Constituent tower energies in positive } \eta, \phi) - \sum (\text{Constituent tower energies in negative } \eta, \phi) \quad (4.3)$$

A jet with all of its energy in the central tower will have  $A_{\eta,\phi} = 0$  whereas a jet of the same energy with all energy deposits in an outer tower will have large  $|A_{\eta,\phi}|$ . If overlapping jets have the same energy, they are instead sorted to give the lowest asymmetry parameter. The first element in the sorted list is then the most energetic jet, with its energy concentrated most centrally within the  $n \times n$  window.

The sorted list is then filtered to remove jets which overlap with this first jet. The process is repeated until 13 separate jets are found. This number is somewhat arbitrary, and is limited by hardware at some high number.

Jets are sorted initially in one dimension, along  $\eta$  or  $\phi$ , and overlaps in one dimension are removed. The resulting list of the most energetic jets along or around the calorimeter is then sorted in the other direction to give the final jet collection.

### 4.3.3 Event-by-event estimation of pile-up

The measurement of the PU contribution to the jet energy is evaluated event by event using a method inspired by the paper of Cacciari and Salam [31] and already used to correct offline jets. In a pp collision with a large number of overlapping proton-proton interactions, a large number of relatively soft jets originate from PU and are distributed roughly evenly across the calorimeter. The median jet transverse energy is therefore very likely to come from PU, and gives a good estimate of the typical transverse energy of a PU jet in the event. Further, the energy density of the median jet transverse energy gives a good estimation of the energy density due to PU across the calorimeter. The energy released by PU per unit area in each event, denoted by  $\rho$ , can therefore be estimated using the median jet transverse energy, and the area of the jet:

$$\rho^{\text{L1}} = \frac{\langle E_{\text{T}}^{\text{L1 jet}} \rangle}{A_{\text{L1 jet}}} \quad (4.4)$$

where  $\langle E_{\text{T}}^{\text{L1 jet}} \rangle$  denotes the median jet transverse energy, and  $A_{\text{L1 jet}}$  denotes the jet area. The energy of all jets in an event can then be corrected for the energy density due to PU

by simply subtracting from all jets in an event using

$$\text{PU corrected } E_T = E_T - \rho^{\text{L1}} \times A_{\text{L1 jet}}, \quad (4.5)$$

because the energy density due to PU across the calorimeter is assumed to be uniform. This assumption is valid for PU values of order  $\sim 50$ , however as PU increases above 100 pp collisions in each bunch crossing, simulation shows many more soft PU jets are expected to lie in the forward regions of the detector, so an  $\eta$  dependent PU subtraction may be more suitable for very high PU scenarios. This is not investigated here, but is within the capabilities of the upgraded trigger system.

In the following we show the effect of PU subtraction in the measurement of the jet energy. The same quantity could also be used to correct contribution of PU to quantities used to defined electrons/photons; isolation parameters, and the ratio of transverse energy deposits in the HCAL and ECAL.

#### 4.3.4 Calibration to the jet energy scale

The raw jet energies from the calorimeter towers must be corrected to the jet energy scale. Different regions of the calorimeter give different responses so a set of calibration constants in  $p_T$  and  $\eta$  are derived. A non linear regression method is used on an independent subsection of 20,000 events collected using single muon trigger; that is, events which contain a least one muon, which often implies hadronic activity in the opposite hemisphere to the muon and so the data sample provides a sufficient number of jets to do a statistically meaningful calibration.

Once the L1 upgrade jets have been created, sorted and filtered, the value of the average energy density due to PU,  $\rho^{\text{L1}}$ , is calibrated to the jet energy scale by comparing it with  $\rho$  calculated offline for each event. The corrected PU subtraction parameter is applied to the L1 jets in the event according to Equation 4.5, in order that they can be calibrated to the offline jets which have been similarly PU subtracted. The leading offline jet in each event, where the jet is formed using the anti- $k_T$  algorithm with radius parameter of 0.5 and inputs from the calorimeter alone, “AK5 Calo jets”, is matched to a L1 jet within a cone of  $\Delta R = \sqrt{(\eta_{\text{L1}} - \eta_{\text{offline}})^2 + (\phi_{\text{L1}} - \phi_{\text{offline}})^2} < 0.5$ . The use of AK5 Calo jets gives reconstructed offline jets as close as possible to those created at L1, as both are built using calorimeter information alone. The values of  $p_T$  and  $\eta$  for the matched L1 and offline jets are used as inputs to a multi-variate analysis. This provides

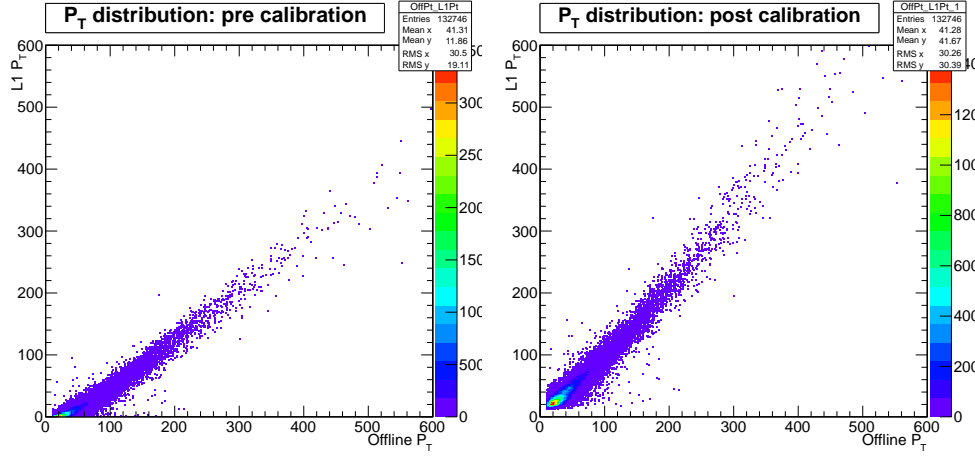


**Figure 4.7:** The  $p_T$  distribution of L1 jets that have been matched, within a cone of  $\Delta R < 0.5$ , to offline jets reconstructed with the anti- $k_T$  algorithm using a radius parameter of 0.5 and calorimeter information as input only. The distribution shown before a  $p_T$  and  $\eta$  calibration has been applied is shown on the left, and after the calibration has been applied on the right. In both distributions, PU has been subtracted from both jet collections.

a lookup table of multiplication factors binned in values of the L1 jet  $\eta$  and  $p_T$ . Applying this calibration to the L1 jets gives a calibration independent of PU.

The distribution of L1 jet  $p_T$ , where each jet has been matched to an offline jet, before and after the calibration has been applied is shown in Figure 4.7. Momenta are much more closely matched after the calibration has been applied.

## 4.4 Upgrade L1 Jet Algorithm Performance

Jet performance can be characterised by angular and energy resolutions, efficiency of reconstruction and trigger rates. The proposed upgrade L1 jets were simulated using data that was collected in high PU conditions during 2012, where events were selected at random from the whole dataset, for example every 10<sup>th</sup> event kept - termed “Zero Bias” data. The LHC run used for the study had an average of 45 primary vertices per bunch crossing.

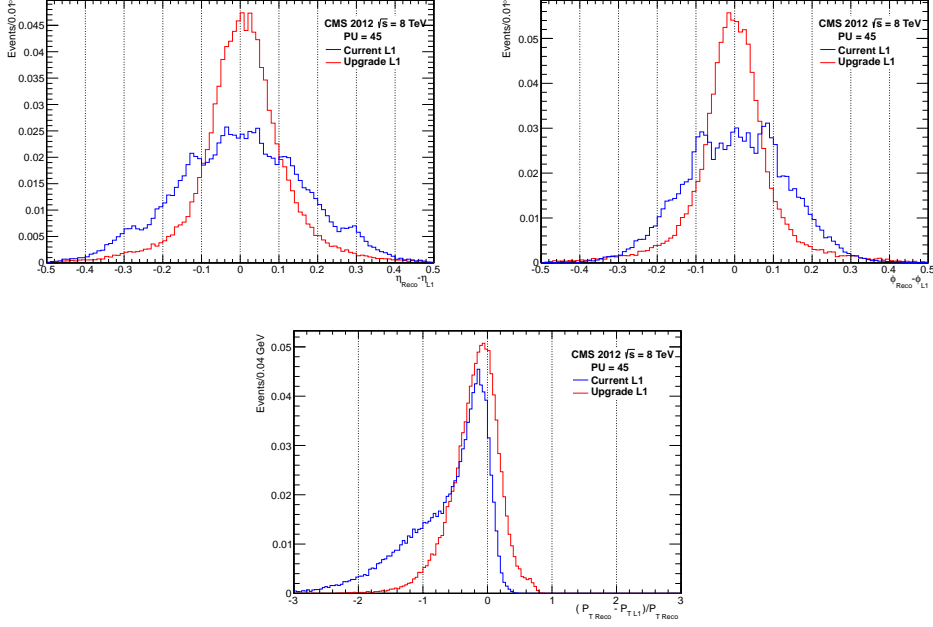


**Figure 4.8:** Resolution of  $\eta$ ,  $\phi$  and  $p_T$  for high PU data taken by the CMS detector in 2012. There is a clear improvement with the upgrade jets, plotted in blue, in both angular resolutions and energy resolution.

#### 4.4.1 Angular and Energy Resolutions

Resolutions are measured as compared to offline AK5 Calo jets, as described in Section 4.3.4. The leading offline jet (which must have  $p_T > 20$  GeV) is matched to a L1 jet within  $\Delta R < 0.5$ , and the resolutions are defined as:

$$\sigma_\eta = \eta_{offline} - \eta_{L1} \quad (4.6)$$

$$\sigma_\phi = \phi_{offline} - \phi_{L1} \quad (4.7)$$

$$\sigma_{p_T} = \frac{p_T^{L1} - p_T^{offline}}{p_T^{offline}} \quad (4.8)$$

Angular and energy resolutions of the proposed upgrade algorithm compared to the current system are shown in Figure 4.8. There is a much improved angular resolution as the upgrade jets take advantage of the full granularity of the calorimeter. In high PU data, the energy resolution is improved due to the PU subtraction. With the current L1 jet algorithm, there are a significant number events in which the leading offline jet has been matched to low energy PU L1 jets, giving a negative value of  $\sigma_{p_T}$  and giving rise to the significant negative tail in the distribution.

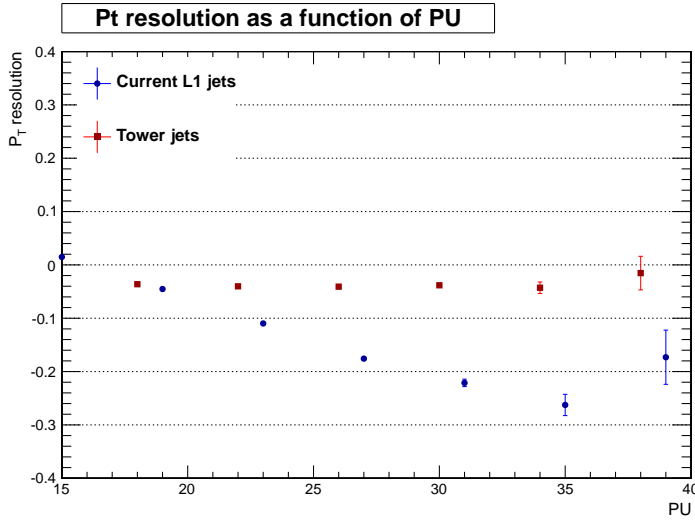


**Figure 4.9:** The PU dependency of the L1 jet energy resolution for both the current algorithm and the upgrade algorithm, where the resolution is taken as the RMS of the PU distribution shown in Figure 4.8, for different PU bins. There is a clear improvement with the upgrade jets, plotted in blue, which shows independence of PU up to PU  $\sim 40$ .

Crucially, the energy resolution of the upgrade jet algorithm shows a much reduced dependence on PU, shown in Figure 4.9. This is evidence that the event-by-event PU subtraction has the intended effect, reducing the worsening effect of additional primary vertices on the jet energy resolution, and the upgrade jet algorithm is therefore expected to show a reduction in rates as compared to the current algorithm.

#### 4.4.2 Trigger efficiencies

The trigger efficiencies for various L1 jet transverse energy thresholds are measured, as compared to AK5 Calo jets, to show the effectiveness of the proposed algorithm at reconstructing jets which have been measured offline, which are treated as the “truth”. If the leading L1 jet in each event above a certain energy threshold is matched to an offline jet, the energy of the matched offline jet is plotted. All matched offline jet energies are also plotted. By taking the ratio between these two distributions we attain trigger turn on curves, shown in Figures 4.10 and 4.11.

The sharpness of the turn on curve is due to the energy resolution of the jet algorithm. If all of the L1 jets have reconstructed energies that exactly equal the energies of the offline jets to which they are matched, i.e.  $\sigma_{p_T} = 0$ , there would be a step function at

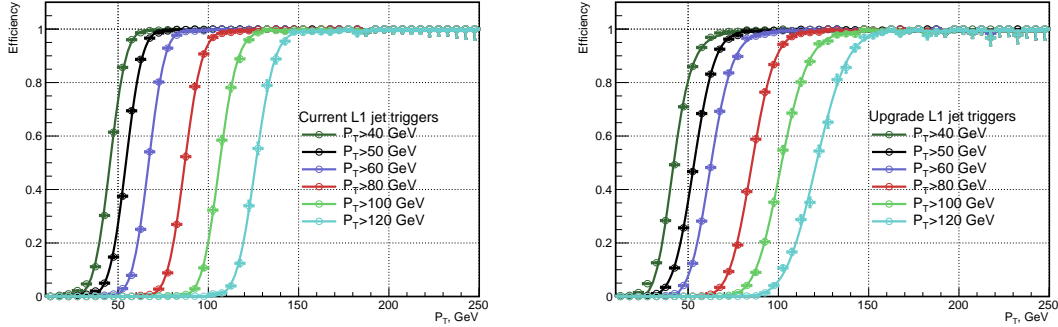


**Figure 4.10:** On the left are the trigger turn on curves for the current jet algorithm and on the right are the trigger turn on curves for the upgrade jet algorithm, for various single jet trigger thresholds, and were calculated using relatively low PU data.

the value of the jet energy threshold of the trigger. The turn on would be instant at the specified trigger threshold. The plateau efficiency of the turn on is dictated by the matching efficiency of the jet algorithm. If all L1 jets are perfectly matched to offline jets then the algorithm is fully efficient at reconstructing jets at L1 and the plateau efficiency is 1.

The turn on curves shown in Figure 4.10 are taken from data taken using the same single muon trigger as was used for jet calibration, where the presence of at least one muon in each event implies there is often hadronic activity in the opposite hemisphere of the detector to the muon. This is a relatively low PU set of events, with approximately 20 p-p interactions per bunch crossing. Figure 4.11 shows the performance at PU of approximately 45, a data sample which has lower statistical precision, hence the larger error bars. The sizeable negative tail shown in the momentum resolution for the current algorithm in Figure 4.8 is evident in the bump at low momentum in the left hand plot. Events in which relatively soft jets due to PU have been reconstructed above threshold at L1 are matched to very soft PU jets reconstructed offline and cause the behaviour at low  $p_T$ . Because the soft PU jets have effectively been removed from the upgrade L1 jet collection, this is not the case for the upgrade trigger turn ons.

The PU subtraction of the proposed upgrade algorithm is also evident in the upward shift in energy of the turn on curves, going from the current algorithm to the upgrade algorithm. For a requirement of, for example, one 40 GeV jet at L1, the offline value at which 95% of events pass the trigger is 51.4 GeV for the current algorithm in the high PU dataset; and 62 GeV for the upgrade algorithm. Table 4.2 shows the offline transverse momentum value at which the trigger is 95% efficient for the various turn on curves

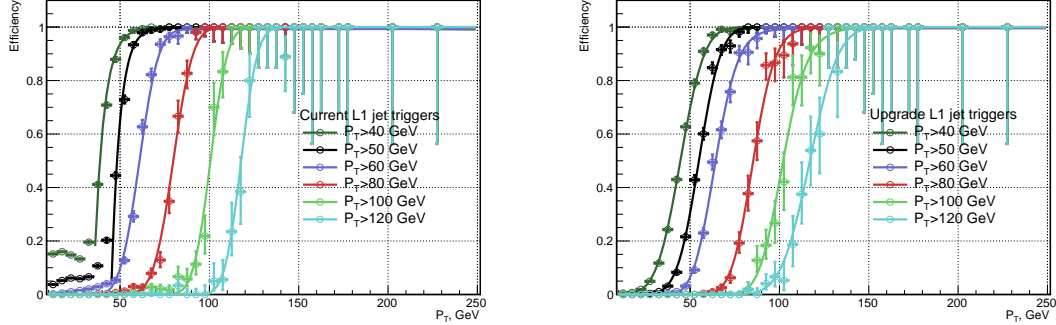


**Figure 4.11:** On the left are the trigger turn on curves for the current jet algorithm and on the right are the trigger turn on curves for the upgrade jet algorithm, for various single jet trigger thresholds, using relatively high PU data.

shown in Figure 4.11. A lower typical hadronic energy at L1 in events reconstructed using the upgrade algorithm, due to the PU subtraction, drives the 95% efficiency values up. Plateau efficiency values are 1 in both algorithms, meaning the upgrade jet algorithm (like the current algorithm) is fully efficient at large jet  $p_T$  values.

**Table 4.2:** The 95% efficiency values for various L1 jet transverse momentum thresholds, in GeV, and plateau efficiency values for the current and upgrade algorithm, for turn on curves taken in high PU data and shown in Figure 4.11.

L1 threshold	Current L1		Upgrade L1	
	95% efficiency	Plateau	95% efficiency	Plateau
40	51.4	1	62.0	1
50	59.5	1	70.9	1
60	75.4	1	83.7	1
80	94.1	1	103	1
100	112.9	1	123.6	1

#### 4.4.3 Jet trigger rates

As discussed in Section 4.1, the purpose of building a new trigger is to be able to better control the trigger rates at reasonable energy thresholds in the future LHC running, which is not possible with the current system. The projected trigger rates of the proposed jet algorithm in the next phases of LHC running are therefore compared to the current

system, in order to show the improvement in rates, and subsequent reduction in energy thresholds possible with the upgraded CMS L1 calorimeter trigger.

Without any requirements on events that are recorded, i.e. Zero Bias data where all events are kept, the rate is equivalent to the instantaneous luminosity multiplied by the inelastic proton-proton cross section,  $R = L \times \sigma_{pp}$ . In events where there are additional primary vertices in the bunch crossing, PU > 1, it takes the number of interacting vertices to get the process in question to occur, so there is an inverse proportionality to the PU,  $R = L \times \sigma_{pp}/PU$ . The rate of events to pass a particular trigger at L1,  $R_{L1}$ , for a given luminosity and PU scenario can then be written as

$$R_{L1} = R_{ev} \cdot \frac{L \times \sigma_{pp}}{PU}, \quad (4.9)$$

where  $R_{ev}$  is the normalised trigger pass rate per event, which for a given set of events is simply the number of events passing a certain trigger divided by the total number of events. Using this equation, the L1 trigger rates can then be extrapolated to a given luminosity and PU scenario.

The rates for several jet triggers are plotted in Figure 4.12, in terms of the L1 jet energy. Usually, the offline cut used in analysis is dictated by the allowed trigger rate, which corresponds to a particular L1 threshold, and therefore to a 95% efficiency value - where the 95% efficiency value is as low as possible to maintain as much phase space as possible (given the rate restrictions). It is therefore also helpful to show the rate in terms of the 95% efficiency, which enfolds both trigger rate and efficiency of the proposed algorithm and enables a fair comparison between the current and proposed upgrade algorithm. The conversion from the online, L1 jet energy to offline 95% threshold is taken from the turn on curves shown in Figure 4.11, using the linear conversion function shown in Figure 4.13. Figure 4.14 shows the single and quad jet (where four jets are required) trigger rates vs the 95% efficiency. The current and upgrade single jet rates are comparable, as the PU subtraction does very little to the leading jet in the event, whereas the multi jet triggers, such as the quad jet trigger, see a significant reduction in rate as PU jets are removed from the event.

#### 4.4.4 Other jet variables

Other offline variables, constructed from jets, have been widely used in the data analyses at CMS at 7 and 8 TeV, both at trigger level and offline. They therefore also will also

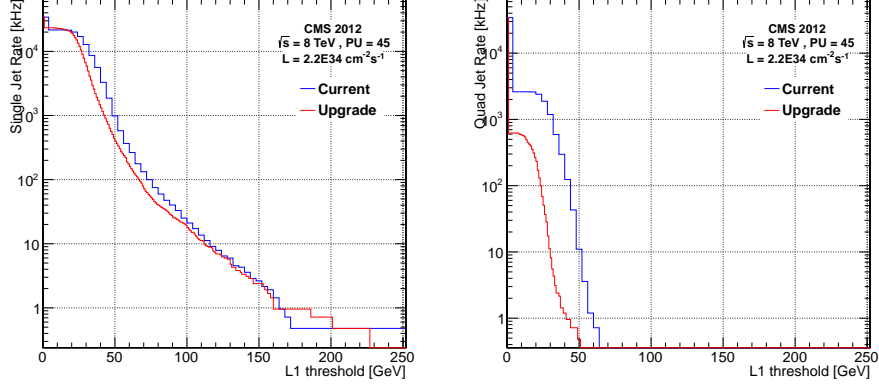


**Figure 4.12:** Rates of single and quad jet triggers. The single jet trigger shows similar performance to the current system, while the multi-jet trigger show a large reduction in rate

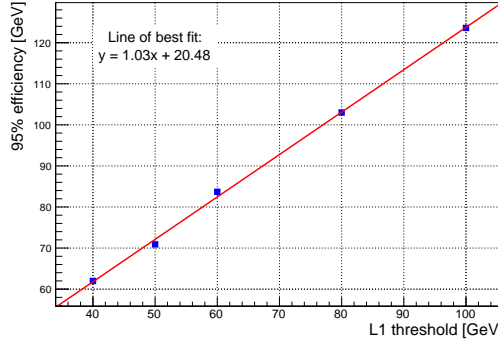


**Figure 4.13:** Conversion between the L1 jet threshold and the 95% efficiency as measured offline, for the proposed upgrade jet algorithm, using the turn on curves shown in Figure 4.11.

benefit from the upgraded calorimeter trigger, and shown here are the improvements in rates for  $H_T$ , the transverse hadronic energy which is defined as the scalar sum of jet transverse momenta in each event:

$$H_T = \sum |p_T^{\text{jet}}| \quad (4.10)$$

where the sum is over all jets in each event.  $H_T$  is commonly used for analysis which search for SUSY, for example in Ref. [32]. It gives a good indication of the amount of hadronic energy in an event and so the energy transfer in the original inelastic p-p collision, which should be high for new physics processes to occur. It is particularly sensitive to the number of primary vertices in each bunch crossing, as soft PU jets are included in the sum. The addition of PU subtraction on an event-by-event basis in

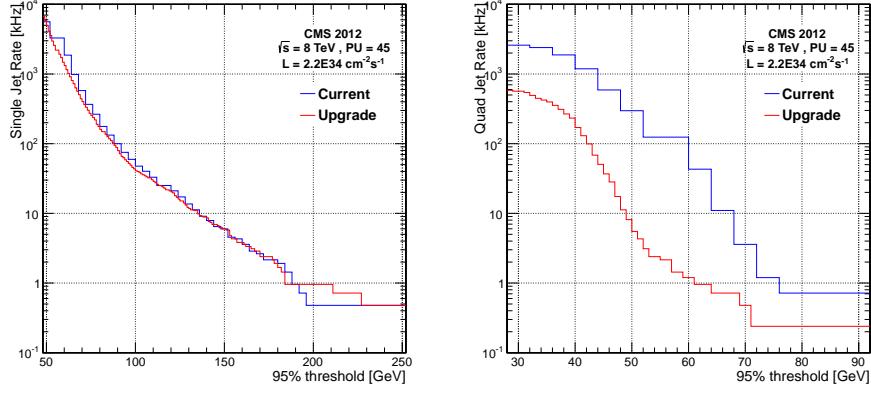


**Figure 4.14:** Rates of single and quad jet triggers. The single jet trigger shows similar performance to the current system, while the multi-jet trigger show a large reduction in rate

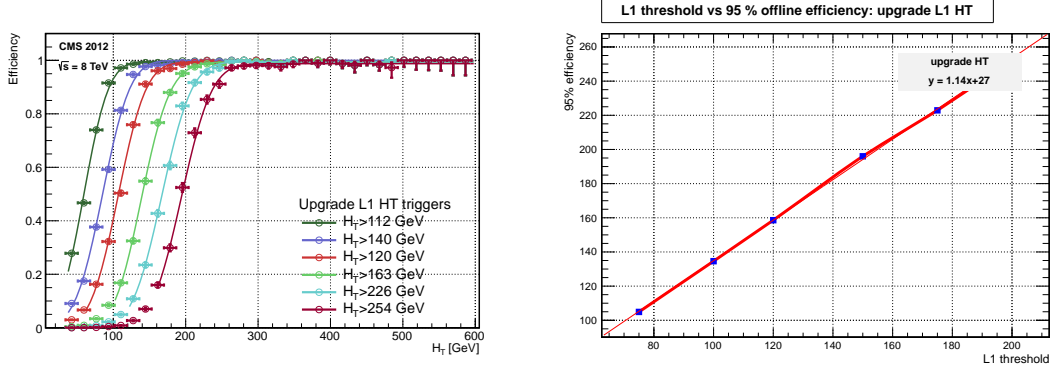


**Figure 4.15:** The trigger turn on curves for the  $H_T$  variable, left, and the conversion between the L1  $H_T$  threshold and the 95% efficiency as measured offline, using  $H_T$  constructed with the proposed upgrade algorithm.

the proposed upgrade jet algorithm therefore has the potential to lead to significant improvements in the rate. The trigger turn on curves for various  $H_T$  thresholds using the upgrade jet algorithm are shown in Figure 4.15 together with the conversion between the L1 threshold and the 95% offline efficiency. The trigger rate of the  $H_T$  in terms of both the L1 threshold and the 95% efficiency are shown in Figure 4.16, which shows a rate reduction of nearly an order of magnitude when using the upgrade algorithm compared to the current algorithm, in terms of the 95% efficiency. This is a much fairer comparison between the two algorithms than the rate in terms of the L1 threshold, as the current  $H_T$  and  $H_T^{\text{miss}}$  values at L1 are not corrected to the jet energy scale.

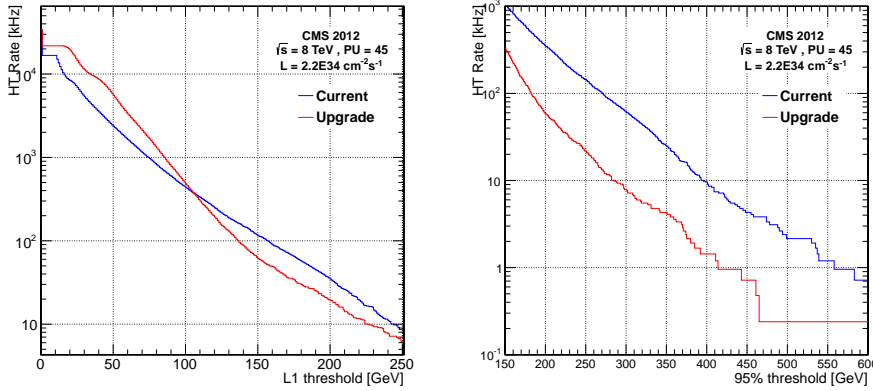


**Figure 4.16:** Rates of  $H_T$  triggers, vs L1 threshold (left) and 95% offline threshold (right), where the conversion between L1 threshold and 95% efficiency is taken from Figure 4.15. There is a significant reduction in rates with the proposed upgrade algorithm.

## 4.5 Conclusion

The proposed upgrade jet algorithm, which is possible to implement with the upgraded CMS calorimeter trigger based upon a TMT architecture, shows significant improvements over the current L1 jet algorithm. By utilising event-by-event PU subtraction at L1 for the first time, the dependency of PU of the L1 jet algorithm is much reduced. By taking advantage of the full tower level granularity of the calorimeter, the angular resolutions of the algorithm are also much improved. This will lead to large improvements in topological calculations at the GT, where two or more objects are used to calculate some quantity which is used in triggering; for example transverse mass, and determining jets arising from Vector Boson Fusion processes such as Higgs boson production. While similar trigger rates are seen for the single jet triggers, there are big improvements in the multijet trigger rates; and a factor of two reduction in the quad-jet trigger rate. The  $H_T$  variable also sees a factor 10 reduction in rate. These rate reductions will allow lower energy thresholds in the upgraded CMS L1 calorimeter trigger, as compared to the current L1 jet algorithm, and help to maintain the energy thresholds and jet rates that were used in 7 and 8 TeV data taking.

This upgrade jet algorithm was proposed in Ref. [28], and the majority work was done during 2012. Many improvements to the algorithm are possible, using different PU subtraction techniques, different jet shapes, and additional parameters such as jet

substructure variables. Indeed, since this work was completed improvements have been made, and documented elsewhere [33].

# Chapter 5

## Searching for Compressed SUSY with monojet events

“”

### 5.1 Analysis

cp PAS.tex .

# Chapter 6

## Searching for Compressed SUSY with monojet events in parked data

Preselection		
Signal region	Dimuon control region	Single muon control region
$E_T^{\text{miss}} > 200 \text{ GeV}$	$E_T^{\text{miss}} > 200 \text{ GeV}$	$E_T^{\text{miss}} > 200 \text{ GeV}$
$p_T(j_1) > 100 \text{ GeV}$	$p_T(j_1) > 100 \text{ GeV}$	$p_T(j_1) > 100 \text{ GeV}$
$N_{\text{jets}} \leq 2$	$N_{\text{jets}} \leq 2$	$N_{\text{jets}} \leq 2$
$\Delta\phi(j_1, j_2) < 2.5$	$\Delta\phi(j_1, j_2) < 2.5$	$\Delta\phi(j_1, j_2) < 2.5$
Veto muon $> 10 \text{ GeV}$	$\mu^+ \mu^-, 60 < m(\mu\mu) < 120 \text{ GeV}$	$1 \mu, 50 < m_T < 100$
Veto electron $> 10 \text{ GeV}$	Veto electron $> 10 \text{ GeV}$	Veto electron $> 10 \text{ GeV}$
Veto had tau (HPS) $> 20 \text{ GeV}$	Veto had tau (HPS) $> 20 \text{ GeV}$	Veto had tau (HPS) $> 20 \text{ GeV}$

**Table 6.1:** Two of the possible luminosity performances for LHC running during Run II, taken from [28].



# Bibliography

- [1] CMS, LHCb Collaboration, “Observation of the rare  $B_s^0 \rightarrow \mu^+ \mu^-$  decay from the combined analysis of CMS and LHCb data”, [arXiv:1411.4413](https://arxiv.org/abs/1411.4413).
- [2] CMS Collaboration, “Summaries of CMS cross section measurements”. <https://twiki.cern.ch/twiki/bin/view/CMSPublic/PhysicsResultsCombined>. Accessed: 2014-12-20.
- [3] S. Weinberg, “A Model of Leptons”, *Phys. Rev. Lett.* **19** (Nov, 1967) 1264–1266, [doi:10.1103/PhysRevLett.19.1264](https://doi.org/10.1103/PhysRevLett.19.1264).
- [4] S. Glashow, “Partial Symmetries of Weak Interactions”, *Nucl.Phys.* **22** (1961) [doi:10.1016/0029-5582\(61\)90469-2](https://doi.org/10.1016/0029-5582(61)90469-2).
- [5] A. Salam, “Weak and Electromagnetic Interactions”, *Conf.Proc.* **C680519** (1968).
- [6] G. Hooft, “Renormalizable Lagrangians for massive Yang-Mills fields”, *Nuclear Physics B* **35** (1971) [doi:http://dx.doi.org/10.1016/0550-3213\(71\)90139-8](https://doi.org/http://dx.doi.org/10.1016/0550-3213(71)90139-8).
- [7] P. Higgs, “Broken Symmetries and the Masses of Gauge Bosons”, *Phys. Rev. Lett.* **13** (Oct, 1964) 508–509, [doi:10.1103/PhysRevLett.13.508](https://doi.org/10.1103/PhysRevLett.13.508).
- [8] ATLAS Collaboration, “Observation of a new particle in the search for the Standard Model Higgs boson with the ATLAS detector at the LHC”, *Phys. Lett. B* **716** (2012) 1, [doi:10.1016/j.physletb.2012.08.020](https://doi.org/10.1016/j.physletb.2012.08.020), [arXiv:1207.7214](https://arxiv.org/abs/1207.7214).
- [9] CMS Collaboration, “Observation of a new boson at a mass of 125 GeV with the CMS experiment at the LHC”, *Phys. Lett. B* **716** (2012) 30, [doi:10.1016/j.physletb.2012.08.021](https://doi.org/10.1016/j.physletb.2012.08.021), [arXiv:1207.7235](https://arxiv.org/abs/1207.7235).
- [10] A. D. M. F. Halzen, “Quarks and Leptons: An Introductory Course in Modern Particle Physics”. John Wiley and Sons, Philadelphia, 1984.
- [11] F. Reines and C. L. Cowan, “The Neutrino”, *Nature* **178** (09, 1956) 446–449.

- [12] M. Gell-Mann, “A Schematic Model of Baryons and Mesons”, *Phys.Lett.* **8** (1964) 214–215, [doi:10.1016/S0031-9163\(64\)92001-3](https://doi.org/10.1016/S0031-9163(64)92001-3).
- [13] G. Zweig, “An SU(3) model for strong interaction symmetry and its breaking. Version 2”,.
- [14] S. Glashow, J. Iliopoulos, and L. Maiani, “Weak Interactions with Lepton-Hadron Symmetry”, *Phys. Rev. D* **2** (Oct, 1970) 1285–1292, [doi:10.1103/PhysRevD.2.1285](https://doi.org/10.1103/PhysRevD.2.1285).
- [15] M. Kobayashi and T. Maskawa, “CP-Violation in the Renormalizable Theory of Weak Interaction”, *Progress of Theoretical Physics* **49** (1973), no. 2, 652–657, [doi:10.1143/PTP.49.652](https://doi.org/10.1143/PTP.49.652), [arXiv:<http://ptp.oxfordjournals.org/content/49/2/652.full.pdf+html>](http://ptp.oxfordjournals.org/content/49/2/652.full.pdf+html).
- [16] ALICE Collaboration, “The ALICE experiment at the CERN LHC”, *JINST* **3** (2008) S08002, [doi:10.1088/1748-0221/3/08/S08002](https://doi.org/10.1088/1748-0221/3/08/S08002).
- [17] ATLAS Collaboration, “The ATLAS Experiment at the CERN Large Hadron Collider”, *JINST* **3** (2008) S08003, [doi:10.1088/1748-0221/3/08/S08003](https://doi.org/10.1088/1748-0221/3/08/S08003).
- [18] CMS Collaboration, “The CMS experiment at the CERN LHC”, *JINST* **3** (2008) S08004, [doi:10.1088/1748-0221/3/08/S08004](https://doi.org/10.1088/1748-0221/3/08/S08004).
- [19] LHCb Collaboration, “The LHCb Detector at the LHC”, *JINST* **3** (2008) S08005, [doi:10.1088/1748-0221/3/08/S08005](https://doi.org/10.1088/1748-0221/3/08/S08005).
- [20] CMS Collaboration, “CMS Physics: Technical Design Report Volume 1: Detector Performance and Software”,.
- [21] M. Cacciari, G. P. Salam, and G. Soyez, “The anti- $k_t$  jet clustering algorithm”, *JHEP* **04** (2008) 063, [doi:10.1088/1126-6708/2008/04/063](https://doi.org/10.1088/1126-6708/2008/04/063), [arXiv:0802.1189](http://arxiv.org/abs/0802.1189).
- [22] CMS Collaboration, “Particle Flow Event Reconstruction in CMS and Performance for Jets, Taus and MET”, CMS Physics Analysis Summary CMS-PAS-PFT-09-001, (2009).
- [23] Aachen-Annecy-Birmingham-CERN-Helsinki-London(QMC)-Paris(CdF)-Riverside-Rome-Rutherford-Saclay(CEN)-Vienna Collaboration Collaboration, “Experimental observation of isolated large transverse energy electrons with associated missing energy at  $\sqrt{s} = 540$  GeV”, *Phys. Lett. B* **122** (Jan, 1983)

- 103–116, [doi:10.1016/0370-2693\(83\)91177-2](https://doi.org/10.1016/0370-2693(83)91177-2).
- [24] Vienna-Wisconsin Collaboration, Aachen-Amsterdam(NIKHEF)-Annecy-Birmingham-CERN-Harvard-Helsinki-Kiel-London(IC)-London(QMC)-MIT-Padua-Paris(CdF)-Riverside-Rome-Rutherford-Saclay(CEN)-Victoria Collaboration Collaboration, “Events with large missing transverse energy at the CERN collider: I.  $W \rightarrow \tau\nu$  decay and test of  $\tau - \mu - e$  universality at  $Q^2 = m_W^2$ ”, *Phys. Lett. B* **185** (Nov, 1986) 233–240, [doi:10.1016/0370-2693\(87\)91561-9](https://doi.org/10.1016/0370-2693(87)91561-9).
- [25] Vienna-Wisconsin Collaboration, Aachen-Amsterdam(NIKHEF)-Annecy-Birmingham-CERN-Harvard-Helsinki-Kiel-London(IC)-London(QMC)-MIT-Padua-Paris(CdF)-Riverside-Rome-Rutherford-Saclay(CEN)-Victoria Collaboration Collaboration, “Events with large missing transverse energy at the CERN collider: II. Search for the decays of  $W^{+-}$  into heavy leptons and of  $Z_0$  into non-interacting particles”, *Phys. Lett. B* **185** (Nov, 1986) 241–248, [doi:10.1016/0370-2693\(87\)91562-0](https://doi.org/10.1016/0370-2693(87)91562-0).
- [26] CMS Collaboration, “CMS The TriDAS Project: Technical Design Report, Volume 2: Data Acquisition and High-Level Trigger. CMS trigger and data-acquisition project”, technical report, Geneva, (2002).
- [27] CMS Collaboration, “Evidence for the direct decay of the 125 GeV Higgs boson to fermions”, [arXiv:1401.6527](https://arxiv.org/abs/1401.6527).
- [28] CMS Collaboration, “CMS Technical Design Report for the Level-1 Trigger Upgrade”, Technical Report CERN-LHCC-2013-011. CMS-TDR-12, CERN, Geneva, (Jun, 2013). Additional contacts: Jeffrey Spalding, Fermilab, Jeffrey.Spalding@cern.ch Didier Contardo, Universite Claude Bernard-Lyon I, didier.claude.contardo@cern.ch.
- [29] R. Frazier, S. Fayer, G. Hall et al., “A demonstration of a Time Multiplexed Trigger for the CMS experiment”, *Journal of Instrumentation* **7** (2012), no. 01, C01060.
- [30] M. Baber, M. Blake, J. Brooke et al., “Development and testing of an upgrade to the CMS level-1 calorimeter trigger”, *Journal of Instrumentation* **9** (2014), no. 01, C01006.
- [31] M. Cacciari and G. P. Salam, “Pileup subtraction using jet areas”, *Phys.Lett. B* **659** (2008) 119–126, [doi:10.1016/j.physletb.2007.09.077](https://doi.org/10.1016/j.physletb.2007.09.077), [arXiv:0707.1378](https://arxiv.org/abs/0707.1378).

- [32] CM Collaboration, “Search for supersymmetry in hadronic final states with missing transverse energy using the variables  $\alpha_T$  and b-quark multiplicity in pp collisions at  $\sqrt{s} = 8$  TeV”, *Eur.Phys.J.* **C73** (2013) 2568,  
[doi:10.1140/epjc/s10052-013-2568-6](https://doi.org/10.1140/epjc/s10052-013-2568-6), [arXiv:1303.2985](https://arxiv.org/abs/1303.2985).
- [33] technical report.

# List of Figures

2.1	Combined results from CMS of many SM measurements made at LHC centre-of-mass energies of 7 and 8 TeV, taken from[2]. Theory and experiment agree over a vast range of production cross section values, for many different SM processes. . . . .	4
3.1	The LHC accelerator ring, showing the locations of the four main experiments at the four collision points. . . . .	9
3.2	The CMS detector, with the main subsystems labelled. . . . .	11
3.3	The CMS tracker, shown in the $rz$ plane. The pixel detector is shown at the centre of the tracker, closest to the interaction region (shown by the black dot), and the strip detector surrounds it. The different subsystems of the strip detector are shown. Taken from Ref.[18]. . . . .	13
3.4	The energy resolution as a function of $ \eta $ for CMS tracker, shown for single muons with $p_T = 1, 10$ and $100$ GeV. . . . .	13
3.5	Geometric view of the CMS ECAL. Barrel crystals are arranged in modules and supermodules, and endcap crystals arranged in supercrystals. Also shown is the preshower detector. . . . .	14
3.6	The energy resolution of an ECAL supercrystal, measured in a test beam. The lower set of points along the dashed line correspond to the energy measured in an array of $3 \times 3$ crystals, where events fall within a $4 \times 4$ mm region in the central crystal. . . . .	15
3.7	Longitudinal view of the CMS HCAL. Locations of the HB, HO, HE and HF are shown with values of $\eta$ . The purple regions represent the muon detectors which further restrict the volume of the HO. . . . .	16

---

3.8	The raw energy response (left) and fractional energy resolution (right) as a function of energy, for pions, in team beam data. . . . .	17
3.9	One of the 5 wheels of the barrel of the CMS muon system. Gaseous detectors are embedded in the iron return yoke of the solenoid; due to the small residual magnetic field in the barrel, DTs are used. . . . .	18
3.10	Muon transverse momentum resolution, shown as a function of muon $p_T$ in the barrel (left) and the endcaps (right). The resolution of the tracker and muon system is shown, and the enhancement gained by combining the information. . . . .	19
3.11	A slice of the CMS detector is shown, with various particles, or physics objects, traversing it. By combining information from each of the subdetectors, each of the particles produced in an event can be identified and the whole event reconstructed. . . . .	20
3.12	The relative insensitivity of the anti- $k_T$ algorithm to PU is shown, compared to other common jet algorithms. The distribution of back reaction, corresponding to the net change in $p_T$ to each of the two hardest jets (where each jet has $p_T > 200$ GeV), when adding PU $\sim 25$ to the event, corresponding to LHC running conditions in the next phase of data taking starting in 2015. Taken from[21]. . . . .	22
3.13	The efficiency of PF jets, and Calo jets, matched to generated jets in the barrel region (left) and the endcap (right), taken from[22]. The superior performance of PF jets is evident because they are more efficiently matched to the generator, “truth” jets, at a lower $p_T$ threshold: termed a sharper turn-on. . . . .	23
3.14	The momentum resolution, $(p_T^{\text{rec}} - p_T^{\text{gen}})/p_T^{\text{gen}}$ of PF jets, and Calo jets, for low energy jets ( $40 \text{ GeV} < p_T < 60 \text{ GeV}$ ) (left) and for high momentum jets ( $300 \text{ GeV} < p_T < 400 \text{ GeV}$ ) (right) in the barrel region, taken from[22]. Not only are the peaks sharper for PF jets, meaning a smaller (and therefore better) overall momentum resolution, but it is also peaking much closer to zero, meaning the jet measurement is much closer to the generated jet momentum. . . . .	23

---

3.15 The momentum resolution, $(E_{T,rec}^{\text{miss}} - E_{T,\text{gen}}^{\text{miss}})/E_{T,\text{gen}}^{\text{miss}}$ of PF and Calo $E_T^{\text{miss}}$ , taken from[22]. An improved resolution is seen using the PF algorithm, particularly at low values of $E_T^{\text{miss}}$ . At higher $E_T^{\text{miss}}$ values, energy measurements are dominated by the calorimeter resolution and values using the two different methods converge. . . . .	25
3.16 Inclusive pp cross sections ( $\sigma$ ) for basic and rarer physics processes, showing some of the phenomena on the physics programme at CMS. Shown on the right are the interaction rates for LHC design luminosity, $10^{34}\text{cm}^{-2}\text{s}^{-1}$ . Taken from[26]. . . . .	26
3.17 Architecture of the L1 trigger. The calorimeter trigger takes inputs from the ECAL, HCAL and HF. The muon trigger takes inputs from the DT, CSCs and RPCs. A decision is made at the L1 GT, using inputs from the GCT and the GMT, of whether to pass an event onto the HLT or discard it. . . . .	28
4.1 The projected L1 trigger menu using the current L1 system and algorithms, at 14 TeV, for illustration purposes. In the left hand column, all of the different triggers contributing to the menu are shown. In the centre (right-hand) columns, the projected L1 trigger rate, 95% threshold and plateau efficiency are shown for running conditions with bunch spacing of 50 ns, $\mathcal{L} = 1.1 \times 10^{34} \text{ cm}^{-2}\text{s}^{-1}$ , PU=50 (25 ns, $\mathcal{L} = 2.2 \times 10^{34} \text{ cm}^{-2}\text{s}^{-1}$ , PU=50), taken from[28]. . . . .	32
4.2 Conventional trigger architecture, showing data processing in regions. Taken from[?]. . . . .	35
4.3 Time-multiplexed trigger architecture, showing data pipelining to different processing nodes. Taken from[?]. . . . .	36
4.4 Layout of trigger towers in the $r - z$ projection, for $0 < \eta < 3.0$ . Both ECAL and HCAL towers are shown. . . . .	38
4.5 Comparison of the current L1 jet map, left, with the proposed upgrade jet map, showing a $8 \times 8$ square jet, right. . . . .	38

4.6 A few of the overlapping jets of one $4 \times 4$ jet (centre, purple), are shown in red. The window of all of the jet overlaps is shown in blue, measuring $10 \times 10$ . These overlapping jets must be sorted and filtered to keep only the most energetic jet. . . . .	39
4.7 The $p_T$ distribution of L1 jets that have been matched, within a cone of $\Delta R < 0.5$ , to offline jets reconstructed with the anti- $k_T$ algorithm using a radius parameter of 0.5 and calorimeter information as input only. The distribution shown before a $p_T$ and $\eta$ calibration has been applied is shown on the left, and after the calibration has been applied on the right. In both distributions, PU has been subtracted from both jet collections. . . . .	42
4.8 Resolution of $\eta$ , $\phi$ and $p_T$ for high PU data taken by the CMS detector in 2012. There is a clear improvement with the upgrade jets, plotted in blue, in both angular resolutions and energy resolution. . . . .	43
4.9 The PU dependency of the L1 jet energy resolution for both the current algorithm and the upgrade algorithm, where the resolution is taken as the RMS of the PU distribution shown in Figure 4.8, for different PU bins. There is a clear improvement with the upgrade jets, plotted in blue, which shows independence of PU up to PU $\sim 40$ . . . . .	44
4.10 On the left are the trigger turn on curves for the current jet algorithm and on the right are the trigger turn on curves for the upgrade jet algorithm, for various single jet trigger thresholds, and were calculated using relatively low PU data. . . . .	45
4.11 On the left are the trigger turn on curves for the current jet algorithm and on the right are the trigger turn on curves for the upgrade jet algorithm, for various single jet trigger thresholds, using relatively high PU data. . . . .	46
4.12 Rates of single and quad jet triggers. The single jet trigger shows similar performance to the current system, while the multi-jet trigger show a large reduction in rate . . . . .	48
4.13 Conversion between the L1 jet threshold and the 95% efficiency as measured offline, for the proposed upgrade jet algorithm, using the turn on curves shown in Figure 4.11. . . . .	48

4.14 Rates of single and quad jet triggers. The single jet trigger shows similar performance to the current system, while the multi-jet trigger show a large reduction in rate . . . . .	49
4.15 The trigger turn on curves for the $H_T$ variable, left, and the conversion between the L1 $H_T$ threshold and the 95% efficiency as measured offline, using $H_T$ constructed with the proposed upgrade algorithm. . . . .	49
4.16 Rates of $H_T$ triggers, vs L1 threshold (left) and 95% offline threshold (right), where the conversion between L1 threshold and 95% efficiency is taken from Figure 4.15. There is a significant reduction in rates with the proposed upgrade algorithm. . . . .	50

# List of Tables

2.1	Summary of the particles of the SM of particle physics. Fermions, of spin- $\frac{1}{2}$ are shown, split into the three generations of leptons and quarks. . . . .	6
2.2	Summary of the gauge bosons of the SM. The force carrying bosons of spin-1 are shown, with the Higgs boson to complete the picture. . . . .	6
4.1	Two of the possible luminosity performances for LHC running during Run II, taken from[28]. . . . .	31
4.2	The 95% efficiency values for various L1 jet transverse momentum thresholds, in GeV, and plateau efficiency values for the current and upgrade algorithm, for turn on curves taken in high PU data and shown in Figure 4.11. . . . .	46
6.1	Two of the possible luminosity performances for LHC running during Run II, taken from[28]. . . . .	53

# 1 Acronyms

<b>ALICE</b>	A Large Ion Collider Experiment
<b>ATLAS</b>	A Toroidal LHC ApparatuS
<b>APD</b>	Avalanche Photo-Diode
<b>ASIC</b>	Application Specific Integrated Circuit
<b>BSM</b>	Beyond Standard Model
<b>CERN</b>	European Organisation for Nuclear Research
<b>CMS</b>	Compact Muon Solenoid

<b>CMSSM</b>	Compressed Minimal SuperSymmetric Model
<b>CSCs</b>	Cathode Stripe Chambers
<b>CSV</b>	Combined Secondary Vertex
<b>CSVM</b>	Combined Secondary Vertex Medium Working Point
<b>CPU</b>	Computer Processing Unit
<b>DAQ</b>	Data Acquisition System
<b>DM</b>	Dark Matter
<b>DT</b>	Drift Tube
<b>ECAL</b>	Electromagnetic Calorimeter
<b>EB</b>	Electromagnetic Calorimeter Barrel
<b>EE</b>	Electromagnetic Calorimeter Endcap
<b>ES</b>	Electromagnetic Calorimeter pre-Shower
<b>EMG</b>	Exponentially Modified Gaussian
<b>EPJC</b>	European Physical Journal C
<b>EWK</b>	Electroweak Sector
<b>FCNC</b>	Flavour Changing Neutral Currents
<b>FPGA</b>	Field Programmable Gate Array
<b>GCT</b>	Global Calorimeter Trigger
<b>GMT</b>	Global Muon Trigger
<b>GT</b>	Global Trigger
<b>HB</b>	Hadron Barrel
<b>HCAL</b>	Hadronic Calorimeter
<b>HE</b>	Hadron Endcaps
<b>HF</b>	Hadron Forward
<b>HLT</b>	Higher Level Trigger

<b>HO</b>	Hadron Outer
<b>HPD</b>	Hybrid Photodetectors
<b>ISR</b>	Initial State Radiation
<b>LUT</b>	Look Up Table
<b>L1</b>	Level 1 Trigger
<b>LEP</b>	Large Electron-Positron Collider
<b>LHC</b>	Large Hadron Collider
<b>LHCb</b>	Large Hadron Collider Beauty
<b>LO</b>	Leading Order
<b>LSP</b>	Lightest Supersymmetric Partner
<b>MC</b>	Monte Carlo
<b>NLL</b>	Next to Leading Logarithmic Order
<b>NLO</b>	Next to Leading Order
<b>NNLO</b>	Next to Next Leading Order
<b>PF</b>	Particle Flow
<b>POGs</b>	Physics Object Groups
<b>PS</b>	Proton Synchrotron
<b>PU</b>	pile-up
<b>QED</b>	Quantum Electro-Dynamics
<b>QCD</b>	Quantum Chromo-Dynamics
<b>QFT</b>	Quantum Field Theory
<b>RBXs</b>	Readout Boxes
<b>RPCs</b>	Resistive Plate Chambers
<b>RCT</b>	Regional Calorimeter Trigger
<b>RMT</b>	Regional Muon Trigger

<b>SLAC</b>	Stanford Linear Accelerator Center
<b>SUSY</b>	SUperSYmmetry
<b>SM</b>	Standard Model
<b>SMS</b>	Simplified Model Spectra
<b>SPS</b>	Super Proton Synchrotron
<b>TIB</b>	Tracker Inner Barrel
<b>TEC</b>	Tracker Endcaps
<b>TID</b>	Tracker Inner Disks
<b>TMT</b>	Time-Multiplexed Trigger
<b>TOB</b>	Tracker Outer Barrel
<b>TF</b>	Transfer Factor
<b>TP</b>	Trigger Primitive
<b>VEV</b>	Vacuum Expectation Value
<b>VPT</b>	Vacuum Photo-Triode
<b>WIMP</b>	Weakly Interacting Massive Particle